Nucleic Acids Research, 2025, **53**, gkaf074
https://doi.org/10.1093/nar/gkaf074
Advance access publication date: 8 February 2025
Gene regulation, Chromatin and Epigenetics

NEAT1-mediated regulation of proteostasis and mRNA localization impacts autophagy dysregulation in Rett syndrome

Edilene Siqueira[1,2], Cecilia D. Velasco[3,4], Ariadna Tarrasón[1], Marta Soler[1], Tara Srinivas[1], Fernando Setién[1], Cristina Oliveira-Mateos[1], Marta Casado-Pelaez[1], Laura Martinez-Verbo[1], Judith Armstrong[5,6,7], Manel Esteller[1,8,9,10], Letícia F. Alves[1], Artur Llobet[3,4], Sonia Guil[1,11,*]

[1]Josep Carreras Leukaemia Research Institute (IJC), Genesis of cancer Program, 08916 Badalona, Catalonia, Spain
[2]Conselho Nacional de Desenvolvimento Cientifico e Tecnológico (CNPq), 70.070-010 Brasilia, Brazil
[3]Laboratory of Neurobiology, Department of Pathology and Experimental Therapy, Institute of Neurosciences, University of Barcelona, 08907 L'Hospitalet de Llobregat, Catalonia, Spain
[4]Bellvitge Biomedical Research Institute (IDIBELL), 08907 L'Hospitalet de Llobregat, Catalonia, Spain
[5]Institut de Recerca Pediàtrica, Hospital Sant Joan de Déu, 08950 Barcelona, Catalonia, Spain
[6]Servei de Medicina Genètica i Molecular, Hospital Sant Joan de Déu, 08950 Barcelona, Catalonia, Spain
[7]CIBER-ER (Biomedical Network Research Center for Rare Diseases), Instituto de Salud Carlos III, 28029 Madrid, Spain
[8]Centro de Investigación Biomedica en Red Cancer (CIBERONC), 28029 Madrid, Spain
[9]Institució Catalana de Recerca i Estudis Avançats (ICREA), 08010 Barcelona, Catalonia, Spain
[10]Physiological Sciences Department, School of Medicine and Health Sciences, University of Barcelona (UB), 08907 Barcelona, Catalonia, Spain
[11]Germans Trias i Pujol Health Science Research Institute, 08916 Badalona, Catalonia, Spain
[*]To whom correspondence should be addressed. Email: sguil@carrerasresearch.org

Abstract

Rett syndrome (RTT) is a severe neurodevelopmental disorder primarily caused by loss-of-function mutations in the *MECP2* gene, resulting in diverse cellular dysfunctions. Here, we investigated the role of the long noncoding RNA (lncRNA) *NEAT1* in the context of MeCP2 deficiency using human neural cells and RTT patient samples. Through single-cell RNA sequencing and molecular analyses, we found that *NEAT1* is markedly downregulated in *MECP2* knockout (KO) cells at various stages of neural differentiation. *NEAT1* downregulation correlated with aberrant activation of the mTOR pathway, abnormal protein metabolism, and dysregulated autophagy, contributing to the accumulation of protein aggregates and impaired mitochondrial function. Reactivation of *NEAT1* in *MECP2*-KO cells rescued these phenotypes, indicating its critical role downstream of *MECP2*. Furthermore, direct RNA–RNA interaction was revealed as the key process for *NEAT1* influence on autophagy genes, leading to altered subcellular localization of specific autophagy-related messenger RNAs and impaired biogenesis of autophagic complexes. Importantly, *NEAT1* restoration rescued the morphological defects observed in *MECP2*-KO neurons, highlighting its crucial role in neuronal maturation. Overall, our findings elucidate lncRNA *NEAT1* as a key mediator of MeCP2 function, regulating essential pathways involved in protein metabolism, autophagy, and neuronal morphology.

Graphical abstract

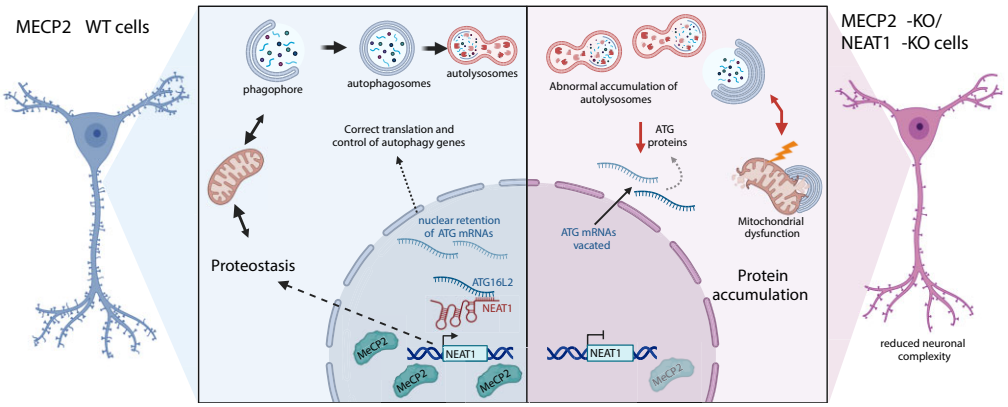

Received: April 29, 2024. **Revised:** January 21, 2025. **Editorial Decision:** January 22, 2025. **Accepted:** January 28, 2025
© The Author(s) 2025. Published by Oxford University Press on behalf of Nucleic Acids Research.
This is an Open Access article distributed under the terms of the Creative Commons Attribution-NonCommercial License (https://creativecommons.org/licenses/by-nc/4.0/), which permits non-commercial re-use, distribution, and reproduction in any medium, provided the original work is properly cited. For commercial re-use, please contact reprints@oup.com for reprints and translation rights for reprints. All other permissions can be obtained through our RightsLink service via the Permissions link on the article page on our site—for further information please contact journals.permissions@oup.com.

Introduction

The methyl-CpG binding protein 2 (MeCP2) is an abundant nuclear protein with global regulatory roles primarily associated with its function as a key epigenetic regulator involved in chromatin remodeling and transcriptional control [1–3]. Initially identified as a protein factor binding to methylated CpG dinucleotides [4], MeCP2 exhibits a complex interactome and participates in gene regulation at multiple levels [3], emerging as a master regulator of various cellular programs. MeCP2 is prominently expressed in the developing brain [5], where it plays critical roles in neural differentiation, maturation, and migration [6, 7]. Loss-of-function mutations in the *MECP2* gene represent the most common cause of Rett syndrome (RTT, OMIM #312750) [8], a severe and progressive neurodevelopmental disorder affecting ∼1 in 10 000 female births [9, 10]. RTT is characterized by sudden regression and subsequent loss of acquired language and motor skills, leading to profound cognitive impairment. Notably, the developmental regression seen in RTT patients arises from altered neural function rather than neurodegeneration. Despite significant progress in understanding MeCP2 function and the pathological consequences of its loss-of-function mutations over the past two decades, a comprehensive understanding linking the nuclear function of MeCP2 with alterations in key signaling pathways and cellular defects in RTT remains elusive. Such in-depth analysis could critically enhance therapeutic interventions, especially as new treatment avenues continue to advance and approach clinical application [11–13].

The study of MeCP2 function has heavily relied on mutant mouse models, which faithfully replicate pathological traits of the disorder, providing comprehensive insights into MeCP2 function across various biological scales, from the cellular to the organismal level [14]. These models can accurately mimic the dendritic and neuronal morphological abnormalities, synaptic imbalances [15, 16], and associated respiratory, motor and cognitive deficits observed in RTT patients [17, 18]. Recent advancements in cell culture technologies [19], coupled with the revolutionary genome editing capabilities of the CRISPR-Cas system [20, 21], have opened new avenues for modeling human disorders *in vitro* with unprecedented precision. Stem cell-based models of RTT have emerged as valuable tools for studying the early stages of the disease, allowing researchers to probe the cellular and molecular underpinnings of MeCP2 loss-of-function in human neurons [22, 23].

Furthermore, single-cell RNA sequencing (scRNA-seq) has emerged as a transformative tool, offering unparalleled insights into the intricate cellular composition, heterogeneity, and dynamics of the developing brain. In contrast to traditional bulk RNA-seq methods, which provide averaged gene expression profiles across cell populations, scRNA-seq offers the resolution needed to dissect heterogeneous cell populations at the individual cell level. This approach unveils a rich transcriptional landscape, unraveling novel cell types, lineage relationships, and regulatory networks pivotal in neurodevelopmental processes, such as neurogenesis, neuronal migration, synaptogenesis, and circuit formation [24]. Additionally, scRNA-seq enables the characterization of cell-to-cell variability, revealing the molecular mechanisms driving cellular diversification and specialization during brain development. For example, recent studies utilizing scRNA-seq have reported high variability in the expression of *MECP2* within inhibitory neurons of the human brain, highlighting both intra- and inter-individual variability [25]. In the context of RTT, an X-linked disorder predominantly affecting females, innovative approaches have been developed to distinguish between cells expressing wild-type (WT) or mutant *MECP2* alleles, enabling the study of mosaic transcriptomic profiles and offering new insights into the pathogenesis of the disorder [26].

In this study, we applied scRNA-seq to dissect the transcriptomic changes in a human cellular model of RTT derived from immortalized neural progenitors [27]. These cells can be differentiated *in vitro* towards different specific subtypes and have been used to model neurodegenerative disorders [28, 29], as well as to investigate MeCP2 function and the impact of its loss-of-function mutations [30, 31]. Our previous research revealed the role of certain types of noncoding RNAs (ncRNAs) in RTT pathophysiology, demonstrating the involvement of specific circular RNAs (circRNAs) and RNAs derived from ultraconserved regions (T-UCRs) in the biogenesis of the ionotropic glutamate receptor of the AMPA type downstream of MeCP2 function [30]. In the present study, we find through scRNA-seq analysis marked downregulation of the evolutionarily conserved, long noncoding RNA (lncRNA) *NEAT1* in *MECP2* knockout (*MECP2*-KO) human neural progenitor and differentiating cells. *NEAT1* plays pivotal roles in nuclear organization, RNA metabolism, and cellular stress responses, with dysregulation of *NEAT1* implicated through unclear mechanisms in various human diseases, including cancer, neurodegenerative disorders, and autoimmune conditions [32–37]. Our findings indicate that *NEAT1* directly regulates the nuclear/cytoplasmic distribution of key autophagy-related messenger RNAs (mRNAs), thereby ensuring proper autophagic flux in response to stress cues. Dysregulation of *NEAT1* is associated with the protein accumulation and autophagic defects observed in *MECP2* mutant cells. Furthermore, reactivation of *NEAT1* in *MECP2*-KO cells rescues the characteristic morphological defects found in RTT neurons, underscoring the contribution of this abundant lncRNA to MeCP2 function and the disease phenotype.

Materials and methods

Post-mortem samples

Post-mortem brain tissue samples were acquired from both control subjects and individuals with RTT. These samples were sourced from the National Institutes of Health NeuroBioBank at the University of Maryland in Baltimore, MD, USA, and the Human Brain and Spinal Fluid Resource Center at the VA West Los Angeles Healthcare Center in Los Angeles, CA, USA. These centers receive sponsorship from the National Institute of Neurological Disorders and Stroke, the National Institute of Mental Health, the National Multiple Sclerosis Society, and the Department of Veterans Affairs.

ReNCells VM cell culture and differentiation methods

Immortalized human neural progenitors [neural progenitor cell (NPC)] from 10-week-old ventral mesencephalon of fetal brain were purchased (ReNCells VM, SCC008, Merck Millipore, Burlington, MA, USA). The cells were cultured in laminin-coated flasks (20 μg/ml; Sigma–Aldrich, St. Louis, MO, USA), with Dulbecco's modified Eagle's medium nutrient mixture (DMEM-F12, L0093-500 Biowest, Nuaillé, France) supplemented with 0.2% heparin (STEMCELL Tech-

nologies, Vancouver, BC, Canada), B-27 complete vitamins (17504-044, Invitrogen, Carlsbad, CA, USA), and antibiotic-antimycotic (L0010-100, Biowest), and kept at 37°C with maximum humidity in an atmosphere of 5% CO_2; media was changed every other day. To maintain pluripotency, basic fibroblast growth factor (bFGF-2) (20 ng/ml, SRP4037) and epidermal growth factor (EGF) (20 ng/ml; SRP3027, Sigma–Aldrich) were added to the feeding media. Cells were split every 3–6 days when 90% confluence was reached using Accutase (SCR005, Sigma–Aldrich), and centrifuged for 5 min at 300 × *g*. For spontaneous differentiation, cells were plated on laminin-coated dishes and allowed to reach 80% confluency, then culture media was administrated without EGF and bFGF-2. Three days after growth factors are withdrawn the cells undergo morphological changes, forming a mixed population of neurons and glia [30]. Glutamatergic differentiation protocol was performed as described previously [30]. Briefly, cells were seeded on laminin-coated plates 24 h before infection. Cells were double infected with TetO-hNGN2-P2A-eGFP-T2A-PuroR and CMV-rtTA. Forty-eight hours after infection, doxycycline (1 μg/ml) was administered to the cells, followed by puromycin (0.5 μg/ml) the next day. After 24 h of puromycin selection, EGF and FGF-2 were withdrawn from the media, and cells were allowed to differentiate for the indicated number of days.

Induced pluripotent stem cells culture and NPC differentiation

RTT patient-derived induced pluripotent stem cells (iPSCs) were kindly donated by the Rett Syndrome Research Trust along with Coriell Institute for Medical Research (Camden, NJ, USA). The cells were sourced from a female RTT patient carrying the T158M mutation on *MECP2* gene. Reprogramming and karyotyping of the cells were performed by the Harvard Stem Cell Institute iPS Core Facility (Cambridge, MA, USA). Two iPSC lines were generated, characterized by random X-inactivation: one is an isogenic control expressing the WT *MECP2*, while the other expresses the T158M mutation. The iPSC colonies were plated on CULTREX™-coated six-well plates (3434-010-02, Bio-Techne R&D Systems) and maintained in mTeSR™1 medium (#85850, STEMCELL Technologies) supplemented with antibiotic-antimycotic (L0010-100, Biowest). They were incubated at 37°C with maximum humidity in a 5% CO_2 atmosphere for 3 days, with daily media changes. Passaging was performed when the cultures reached 80% confluency, using Gentle Cell Dissociation Reagent (STEMCELL Technologies). On day 4, iPSC colonies were dissociated into single cells and plated for NPC differentiation on CULTREX™-coated six-well plates, following the monolayer method and the dual Suppressor of Mothers Against Decapentaplegic (SMAD) inhibition-mediated neural induction protocol (#08581, STEMdiff™ SMADi Neural Induction Kit, STEMCELL Technologies), as per the manufacturer's instructions. Media were changed daily, and cells were passaged three times during the 21-day protocol. Cell pellets were collected at the undifferentiated stage (as stem cells expressing NANOG and OCT4) and at various stages of differentiation (days 5, 8, and 11). Differentiation into NPCs was confirmed by the expression of SOX1 and PAX6 (see the 'Immunofluorescence' section for details).

Single-cell RNA sequencing

Two scRNA-seq experiments were performed. In experiment 1, WT and *MECP2*-KO (clone A33) cells were cultured and differentiated in a time-course for the experiment: progenitors, 3, 7, 14, 21, and 30 days after differentiation. At each time point, cells were pooled and separated by fluorescence-activated cell sorting (FACS). FACS conditions and cellular selection were optimized beforehand to ensure neuron viability post-sorting. scRNA-seq was carried out at CNAG (CRG, Barcelona, Spain), using the following protocol. The cellular concentration and viability were verified by counting with a TC20™ Automated Cell Counter (Bio-Rad Laboratories, S.A.). Individual cells were partitioned into Gel Bead-In-Emulsions with a Target Cell Recovery of 5000 total cells, by using the Chromium Controller system (10X Genomics). Complementary DNA (cDNA) sequencing libraries were prepared using the Chromium Single-cell 3′ mRNA kit (V3; 10X Genomics) following manufacturer's instructions. Briefly, after GEM-RT clean up, cDNA was amplified during 13 cycles and cDNA QC and quantification were performed on an Agilent Bioanalyzer High Sensitivity chip (Agilent Technologies). Libraries were indexed via polymerase chain reaction (PCR) with the PN-220103 Chromium i7 Sample Index Plate. Final cDNA library size and concentration were confirmed using the same Bioanalyzer system. Sequencing was carried out on a NovaSeq 6000 platform (Illumina), producing ∼40 000 paired-end 50 bp reads per cell.

In experiment 2, WT, *MECP2*-KO A33 and *MECP2*-KO 3F cells were cultured and collected as progenitors (pg) and after 7 days of differentiation (7d). Cells were pooled and separated by FACS. Sample preparation and scRNA-seq were performed by the Single Cell Unit (Josep Carreras Research Institute, Badalona, Spain) and Macrogen, Inc. (Seoul, Republic of Korea), following the same protocol described for experiment 1.

For both experiments, data analysis was conducted using the Seurat package version 5.0.1 in R version 4.3.2. Cells were filtered based on the number of unique genes detected, the total number of molecules detected, and the mitochondrial content. The number of cells analyzed per condition for each experiment was: experiment 1 – WT: pg (10 169), 7d (11 216); MECP2-KO A33: pg (9936), 7d (10 604); MECP2-KO 3F: pg (8956), 7d (10 678); experiment 2 – WT: pg (10 169), 7d (11 216); MECP2-KO A33: pg (9936), 7d (10 604); MECP2-KO 3F: pg (8956), 7d (10 678). Expression data were normalized using the *LogNormalize* function and scaled with *ScaleData*. Highly variable genes were identified with the *FindVariableFeatures* function. Dimensionality reduction was performed using principal component analysis, retaining the first 20 principal components. Clustering was performed using *FindNeighbors* and *FindClusters*, and clusters were visualized with Uniform Manifold Approximation and Projection (UMAP). Cell cycle phases were scored using the *CellCycleScoring* function, and cells were classified into NEAT1 high and low expression groups based on the 60th percentile. Differential gene expression analyses were performed with the *FindMarkers* function (Wilcoxon Rank Sum test, min.pct = 0.1. An astrocyte gene signature was computed using the *AddModuleScore* function, based on the expression of the following genes: AQP4, ALDOC, S100B, CD44, NF1A, SLC1A3, SLC1A2, CX43, VIMENTIN, and ALDH1L1.

Total RNA sequencing

Total RNA was extracted with Promega's Maxwell RSC microRNA (miRNA) Tissue kit (AS1460, Promega, Madison, WI, USA). RNA-seq libraries were generated and sequenced by BGI (Warsaw), in 150-bp paired-end, with the DNBSEQ platform, using three biological replicates for each group, with an average yield of 13.27G data per sample. Fastq files were aligned to the hg38 transcriptome using HISAT, with standard options. Clean reads were aligned to the reference genes using Bowtie2. Differentially expressed genes were detected with DESeq2. Only genes with an absolute $\log_2$FC > 1 and a q value < 0.05 were selected as differentially expressed.

Transmission electron microscopy

Plastic cover slips (Thermanox, Thermo Fisher Scientific, Waltham, MA, USA) were coated with laminin and placed in 12-well plates. Progenitor cells were plated the day before the experiment. The next day the cells were fixed with 1.8% glutaraldehyde solution (#16216, Electron Microscopy Sciences) in 0.1 M cacodylate buffer (pH 7.4; #11650, Electron Microscopy Sciences), and then the wells were washed three times with 0.1 M cacodylate buffer for 5 min each. Next, the covers were incubated with 1% osmium tetroxide/1.5% potassium ferricyanide solution for 1 h on ice. Covers were incubated with 1% tannic acid in 0.05 M sodium cacodylate at room temperature (RT) for 45 min, and then washed and dehydrated in an ethanol series. The samples were then embedded in Epon resin mixed with propilene oxide (1:1) for 30 min, followed by fresh 100% Epon for 1 h. The cover slips were placed on solid Epon Beem capsules and baked at 60°C overnight to polymerize the resin. Ultrathin (60–70 nm) sections (Ultracut Reichert S, Leica) were collected on 200 mesh copper grids and contrasted with 2% uranyl acetate in methanol and 0.5% lead citrate in aqueous solution. Ultrastructure images were captured with a transmission electron microscope (JEOL 1010, operated at 60 kV). The number of endosomes and mitophagy events was measured in micrographs obtained at 8000–20 000 magnifications (n > 30 micrographs per sample).

Generation of knockout and mutant cell lines [*MECP2*-KO (clones A33 and 3F), *MECP2*-R133C, and *NEAT1*-KO]

CRISPR/Cas9 technology was used for engineering *MECP2* and *NEAT1* knockouts (KOs) and for introducing the *MECP2*-R133C point mutation in human ReNCells VM. For details on the generation of the *MECP2*-KO A33 clone, refer to Siqueira *et al.* [30]. The MECP2-KO 3F clone was created using a guide RNA targeting exon 4 (5′-AAAAGCCTTTCGCTCTAAAG-3′), designed with the CRISPR Design Tool (http://crispr.mit.edu/), and cloned into the pSpCas9 (BB)-2A-GFP vector (PX458, Addgene® #48138, Watertown, MA, USA).

The *MECP2*-R133C cell line was generated by introducing a cytosine-to-thymine substitution at position g.105697C > T on chr X of the genomic DNA using a donor sequence (5′-CTCTGACATTGCTATGGAGAGCCTCTAATTGTTCC TTGTGTCTTTCTGTTTGTCCCCACAGTCCCCAGGGA AAAGCCTTTTGCTCTAAAGTGGAGTTGATTGCGTAC TTCGAAAAGGTAGGCGACACATCCCTGGACCCTAAT GATTTTGACTTCACGGTAAC-3′). The guide RNA mentioned above was used to create a double-strand DNA break, while the donor sequence provided the template to introduce the R133C missense mutation.

NEAT1 KO was achieved using a construct described by Li *et al.* [38]. The pX330-NEAT1pr_v1 plasmid [gift from Archa Fox (Addgene plasmid #97082; http://n2t.net/addgene:97082; RRID: Addgene_97082)] encodes Cas9 protein and a single guide RNA targeting the human *NEAT1* promoter region. For all the above cell line generation, ∼2 million cells were transfected by nucleofection (A33 voltage, VPI-1003, Primary Neurons Kit, Amaxa®, Lonza Group Ltd, Basel, Switzerland) with their corresponding plasmids. *MECP2*-KO clones A33 and 3F were isolated by FACS. *NEAT1*-KO cells correspond to the pool of transfected cells. *MECP2* depletion was confirmed by western blotting (WB) and Sanger sequencing, while *NEAT1* depletion was validated by reverse transcription quantitative polymerase chain reaction (RT-qPCR) and RNA fluorescence *in situ* hybridization (RNA-FISH). The missense mutation was confirmed by Sanger sequencing.

NEAT1-shRNA depletion

Short-hairpin RNAs (shRNAs) targeting the *NEAT1* gene (isoforms 1 and 2) were selected based on published sequences [39, 40] and screened for potential off-target effects. Two distinct shRNAs (shRNA1 and shRNA2, Supplementary Table S2) were cloned into the BamHI and EcoRI restriction sites of the pLVX-shRNA2 vector (Cat# 632179, Clontech). Lentivirus production was performed in HEK293T cells, maintained in DMEM with GlutaMAX (Cat# 31966-021, Thermo Fisher Scientific) supplemented with 10% fetal bovine serum (Cat# 10270, Thermo Fisher Scientific), at 37°C in a 5% CO_2 atmosphere. HEK293T cells were co-transfected with the shRNA vectors and packaging plasmids using jetPRIME® transfection reagent (Cat# 114-15, Polyplus-Transfection) following the manufacturer's protocol. Forty-eight hours post-transfection, the culture supernatant containing lentiviral particles was collected, filtered through a 0.45 μm low-protein-binding filter, and concentrated using Lenti-X Concentrator (Cat# PT4421-2, Clontech). The concentrated lentiviral particles were stored at −80°C until use. For viral transduction, target cells were infected with the lentivirus, and a 2-day recovery period was allowed before initiating downstream experiments.

NEAT1 reactivation/overexpression

NEAT1 expression was reinstated in human *MECP2*-KO and *NEAT1*-KO cells using two distinct strategies: CRISPR activation technology and the introduction of the cloned long isoform of *NEAT1*. The CRISPR activation method employed a catalytically inactive Cas9, as outlined by Yamazaki *et al.* [41]. For this approach, we used the following three plasmids: single-guide RNA (sgRNA) [MS2; a guide cloning backbone (Plasmid #61424)], dCAS9-VP64_GFP (Plasmid #61422), and MS2-P65-HSF1_GFP (Plasmid #61423), which were acquired from Addgene (Watertown, MA, USA). Lentiviruses for dCAS9-VP64_GFP and MS2-P65-HSF1_GFP were produced as described above. For the sgRNAs delivery, three sgRNAs targeting the promoter region of *NEAT1* (listed in Supplementary Table S2) were synthesized and cloned into sgRNA (MS2). *MECP2*-KO and WT cells that had been previously infected were seeded in 10-cm dishes and transfected with Lipofectamine™ Stem Transfection Reagent (Thermo Fisher Scientific). Overexpression of *NEAT1* was verified by

RT-qPCR. As control, WT and *MECP2*-KO cells were transfected with the empty vector.

MALAT1 and *NEAT1* long isoform cloning

Isoform 1 of human *MALAT1* (NR_002819.4, 8779 bp) was cloned into the pcDNA4/TO vector (Clontech, Mountain View, CA, USA) using BsiWI and NotI restriction sites. The 8779 bp sequence, along with 100 bp of downstream genomic DNA, was amplified from ReNCells VM DNA using high-fidelity Phusion DNA Polymerase. Primers containing BsiWI and NotI sites were designed (Supplementary Table S2). The entire sequence was confirmed by Sanger sequencing to ensure fidelity. The long isoform of human *NEAT1* (*NEAT1_2*, NR_131012.1, 22 kb) was successfully cloned into the pcDNA4/TO vector (Clontech, Mountain View, CA, USA). Initially, the 5′ region of NEAT1, spanning ∼3 kb, was amplified using the plasmid pCRII_TOPO_hNEAT1 [a gift from Archa Fox [42] (Addgene plasmid #61518; http://n2t.net/addgene:61518; RRID: Addgene_61518)] as a template. Subsequently, the remaining 19 kb segment of the *NEAT1* sequence was amplified from ReNCells VM cDNA in two separate PCRs, employing high-fidelity Phusion DNA Polymerase for enhanced accuracy. These PCR products were then assembled and cloned into the pcDNA4/TO vector at the AscI and BamHI restriction sites, creating a comprehensive 22 kb *NEAT1* insert. To ensure fidelity of cloning processes, the entire PCR-amplified fragment underwent sequencing, confirming the integrity of the sequence and the absence of PCR-induced mutations. However, for *NEAT1_2*, sequence analysis revealed a 903 bp deletion within the 3′ region of *NEAT1* [chr11:65 436 667–65 437 571 (hg38)]. This deletion was consistently observed in the cDNA from multiple cell lines, suggesting a biological origin rather than a cloning artefact. Moreover, attempts to amplify this genomic region were unsuccessful, indicating potential annotation inaccuracy, or technical challenges associated with its sequence complexity or structure.

For the introduction of the constructed vector into cells, Neon NxT Electroporation (Thermo Fisher Scientific) was utilized. Cells were first detached using Accutase® and subsequently counted. Two million cells were then suspended in 100 µl of electroporation buffer, together with 5 µg of the plasmid, and electroporated under the following conditions: 1400 V for 20 ms, delivered in two pulses. Post-electroporation, cells were cultured in media supplemented with RevitaCell® (Thermo Fisher Scientific) to enhance recovery, with a media change performed the following day. The successful overexpression of *NEAT1* was ascertained using ViewRNA assays, confirming the effectiveness of the cloning and delivery strategy. The empty vector and the vector containing cloned *MALAT1* were used as experiment controls.

RNA in situ hybridization

ReNCells VM were seeded onto laminin pre-treated eight-well chambers one day before the experiments or allowed to differentiate for 7 days. Cells were probed for single-molecule sensitivity using the ViewRNA Cell Plus Assay kit (Ref. 88-19000-99, Thermo Fisher Scientific) following the manufacturer's instructions. In brief, cells were fixed and immunostained overnight with Nestin antibody (for cytoplasmic determination) and secondary antibody Alexa FluorTM 488 chicken anti-mouse (1:1000, #A-21200, Thermo Fisher Scientific). RNA molecules, including ATG16L1 type 6 (VA6-3181792-01VX-01), ATG16L2 type 6 (VA6-3178559-01VX-01), MALAT type 6 (VA6-14180-VCP), ATG5 type 6 (VA1-12125-VC VX-06), NEAT1 type 6 (VA6-14476-VCP VX-06), or type 1 (VA1-12621-VCP), were probed, followed by pre-amplification, amplification, and probe labeling in a HybEZ™ II Oven (Advanced Cell Diagnostic, San Francisco, CA, USA) as per the manufacturer's recommendations. Nuclei were stained with 4′,6-Diamidino-2-Phenylindole (DAPI). Slides were mounted using FluorSave™ Reagent (345 789, Merck Millipore), dried overnight at room temperature in the dark, and finally stored at 4°C. Images of hybridized cells were captured the following day using a Zeiss Axio Observer Z1 fluorescent microscope with ZEN blue 2012 software (Zeiss, Jena, Germany) and analyzed with ImageJ v1.51h. ImageJ software (v1.51h) was used to quantify the signal intensity of *MALAT1* and the number of *NEAT1* + foci per nucleus. For signal intensity analysis, DAPI staining was used to define the nuclear area (region of interest, (ROI)), and the *MALAT1* fluorescence intensity was measured in multiple nuclei per image ($n > 9$) across several fields ($n = 5$ images). The *MALAT1* signal intensity ratio was calculated by normalizing fluorescence intensity to the nuclear area. For *NEAT1* + foci quantification, the counting tool in ImageJ was employed, analyzing all visible nuclei ($n > 9$ per image) across at least seven images per cell type. The distribution of *NEAT1* + foci was presented as a percentage of the total, or as a distribution plot.

Immunofluorescence

For NeuronStudio analysis and immunofluorescence (IF), ReNCells VM cells were plated on laminin-coated eight-well chambers (Merck Millipore) and iPSC were plated on CULTREX™-coated 18-mm glass slides. The differentiation procedure was the same as previously described. On the day of the experiment, cells were fixed with 4% paraformaldehyde (Electron Microscopy Sciences) in washing solution [1 mM NaCl, 1 mM $MgCl_2$ in phosphate-buffered saline (PBS), pH 7.4] for 20 min at RT. Each chamber was blocked with 5% bovine serum albumin and 5% goat serum (Sigma–Aldrich) in 0.3% Triton® in washing solution for 1 h at RT. Primary antibodies (Supplementary Table S1) were diluted in blocking solution and incubated overnight (12–16 h). Secondary antibodies (dilution 1:1000) were incubated for 1 h at room temperature in the dark (Supplementary Table S1). Chambers were washed between steps with washing solution three times for 5 min each. DAPI (5 mg/ml) was used for nuclei staining. Chambers were then removed from support, slides were mounted in FluorSave™ reagent (Merck Millipore), and dried overnight at room temperature, protected from light. Images were acquired with a Zeiss Axio Observer Z1 fluorescent microscope with ZEN blue 2012 software (Zeiss, Jena, Germany), and were analyzed in ImageJ software (v1.53k). Signal Intensity was measured using ImageJ software (v1.51h).

Autophagy flux assay

FUW mCherry-GFP-LC3 was a gift from Anne Brunet [43] (Addgene plasmid #110060; http://n2t.net/addgene:110060; RRID: Addgene_110060). LC3-GFP-mCherry lentiviral particles were produced in HEK293T cells as mentioned previously. For infection, ReNCells VM (WT, *MECP2*-KO, and NEAT1-KO cells) were seeded in laminin-coated flasks until they reached 70% confluency, at which point the virus

concentration for infections was optimized in order to obtain optimal fluorescence signals. Following confirmation of Green Fluorescent Protein (GFP) and mCherry expression via microscopy, the cells were transferred to laminin pre-coated eight-well chambers and treated with Bafilomycin A1 (Selleckchem, Catalog No. S1413) for 16 h. The cells were then fixed with 4% Paraformaldehyde (PFA) in PBS for 10 min and washed three times with PBS. Nuclei were stained with DAPI. The cells were mounted in FluorSave™ reagent (Merck Millipore) and left to dry overnight at room temperature, shielded from light. Images were taken using a Leica Stellaris 8 microscope. Quantification was performed by counting the number of green and red foci in the images ($n > 10$ cells). Overlapping signals were identified by merging the corresponding channels. The analysis was conducted using the 'Cell Counter' plugin in ImageJ software (version 1.51 h).

Rapamycin and autophagy inhibitors treatment

For autophagy modulation, cells were seeded one day prior to treatment and cultures under optimal growth conditions, with strict adherence to prevent confluency from surpassing 80%. Cells were treated with Rapamycin (an mTOR inhibitor) at 50 μM, and Bafilomycin A [an inhibitor of vacuolar-type H (+)-ATPase] at a concentration of 10nM for 16h. Parallel control groups were subjected to treatment with the corresponding vehicle control (DMSO) ensuring that Dimethyl Sulfoxide (DMSO) levels did not exceed 0.5% of the total culture volume. Evaluation of treatment efficacy was conducted with WB through analysis of LC3 or S6 phosphorylation levels. Further details can be found in the WB section.

RNA extraction and RT-qPCR

Total RNA was extracted with Promega's Maxwell RSC miRNA Tissue kit (AS1460, Promega, Madison, WI, USA). A negative control minus reverse transcriptase was run in parallel to control for genomic contamination. Real-time PCR reactions were performed in triplicate with a QuantStudio™ 5 Real-Time PCR System (TermoFisher Scientific, Waltham, MA, USA), using 10–30 ng of cDNA, 6 μl SYBR® Green PCR Master Mix (Applied Biosystems, Foster City, CA, USA), and 416 nM primers in a final volume of 12 μl for 384-well plates. All data were acquired and analyzed with the QuantStudio Design & Analysis Software v1.3.1 and normalized with *L13* as endogenous control. Relative RNA levels were calculated using the comparative Ct method (ΔΔCt). A list of the primers used can be found in Supplementary Table S2.

Western blotting

Fresh cellular pellets from progenitors and 7 day-differentiated cells (>2 × 10^6 cells) were scrapped and proteins extracted with Laemmli buffer [2% sodium dodecyl sulphate (SDS), 10% glycerol, 60 mM Tris–Cl, pH 6.8, 0.01% bromophenol blue], sonicated, and boiled for 5 min at 95°C after β-mercaptoethanol addition (2% final concentration). Samples' concentration was determined quantifying the absorbance at 260 nm with the NanoDrop™ One/OneC Microvolume UV Spectrophotometer and using the equivalency between DNA and histones [6 units A_{260nm} (DNA) = 1 μg/μl of protein]. Equal amounts of protein (20 μg up to 40 μg) were loaded in 6%–15% sodium dodecyl sulphate–polyacrylamide gel electrophoresis gels and separated by electrophoresis. Next, samples were transferred to nitrocellulose membranes (0.2 μm), for 1 h with <400 mA. Blocking was performed for 1 h at RT with 5% skimmed milk with 0.1% Tween 20® in PBS buffer. Primary antibodies (Supplementary Table S1) were diluted in blocking solution and incubated overnight at 4°C in a shaker. Membranes were washed between incubations with 0.1% Tween 20® in PBS buffer three times for 7 min each. Secondary antibodies conjugated to horseradish peroxidase (HRP) anti-rabbit IgG (1:10 000; A0545; Sigma–Aldrich) or anti-mouse IgG (1:5000; NA9310, GE HealthCare, Chicago, IL, USA) were incubated for 1 h at RT in slow shaking. Lastly, bands were visualized using an ECL detection kit (GE Healthcare Life Sciences). ß-Actin-HRP (45 kDa, Sigma, #A5441) and α-TUBULIN-HRP (55 kDa, Abcam, Cambridge, UK, ab40742) were used as loading control. Protein abundance in each blot was quantified and is displayed below each western blot panel as the mean relative percentage compared to the control condition, normalized to the loading control. Ponceau staining was also performed to verify the accuracy and consistency of sample loading. Chemiluminescence signal intensity was quantified automatically using iBright software, expressed as signal intensity density for each membrane ($n = 3$). Supplementary Table S3 presents the mean values ± standard deviation (SD) from two biological replicates and 1–2 technical replicates for all WB panels.

Proteostat

Protein aggregates were quantified using the ProteoStat® Aggresome Detection kit, adhering to the manufacturer's protocol (Enzo Life Sciences, Farmingdale, NY). Cells grown under standard conditions were detached with Accutase and centrifuged at 300 × *g* for 5 min. Following a PBS wash, the cells were resuspended in 1 ml of PBS. They were then fixed with cold 4% paraformaldehyde for 30 min, centrifuged at 400 × *g* for 10 min, and washed with PBS to eliminate any paraformaldehyde residue. Subsequently, cells were permeabilized with 0.5% Triton X-100 for 15 min and stained with ProteoStat aggresome dye at a 1:2 500 dilution. Aggresomes were analyzed using a BD FACSCanto™ II Flow Cytometer (BD Biosciences) equipped with a 488-nm laser, detecting fluorescence in the PE channel. Data collection utilized gating criteria to isolate viable, single cells, using forward scatter (FSC) and side scatter (SSC) for selection.

Mitochondrial function analysis

Cells were seeded 24 h prior to the experiment on laminin pre-coated 12-well plates and grown under standard conditions. Live cells were treated with Tetramethylrhodamine, Ethyl Ester (TMRE) (T669, Invitrogen, Carlsbad, CA, USA) at a concentration of 50 nM for 30 min at room temperature, Bio Tracker ATP (SCT045, Merck Millipore) at a concentration of 7.5 μM for 15 min at 37°C, or MitoSOX™ (M36008 Thermo Fisher Scientific) at a concentration of 5 μM for 10 min at 37°C. Simultaneously, mitochondria were dyed with green MitoTracker™ (M7514, Thermo Fisher Scientific) at a concentration of 100 nM for 30 min RT in accordance with the manufacturer's recommendations. Following a 1-h exposure to MitoTracker, cells were detached using Versene (15040-033, Gibco®, Thermo Fisher Scientific). The detached cells were collected with PBS and subsequently centrifuged at 300 × *g* for 5 min. The resulting pellet was subjected to a single wash in PBS, followed by centrifugation

under the aforementioned conditions. The cell population was resuspended in 200 µl of PBS and analyzed by flow cytometry using a FACSCantoII Flow Cytometer (BD Biosciences, CA, USA) equipped with a 488-nm laser and fluorescence detection in the Phycoerythrin (PE) and Allophycocyanin (APC) channels. Data acquisition was performed, employing gating parameters to select viable, single cells based on FSC and SSC. Fluorescence signals for MitoTracker™ and TMRE were acquired, with compensation adjusted as necessary to correct for spectral overlap. Only MitoTracker™-positive cells were considered in the subsequent analytical assessments.

Nuclear and cytoplasmic fractionation

Subcellular fractionation was carried out utilizing a PARIS™ kit (#AM1921, Thermo Fisher Scientific) in accordance with the manufacturer's instructions. Equivalent quantities of cDNA from each fraction were subjected to RT-qPCR, and the results were standardized by considering the total RNA quantity obtained from each fraction. Endogenous control primers for MALAT1 and GAPDH were used to validate the segregation of mRNA into nuclear and cytoplasmic fractions, respectively. To validate the separation at the protein level, a western blot was conducted using antibodies against HISTONE H3 (1:5000, ab1791, Abcam) and α-TUBULIN-HRP (1:5000; ab40742, Abcam).

RNA pull-down and RIP-sequencing

NEAT1 RNA pull-down was performed as described previously [44, 45], with some modifications. Cells were plated on laminin-coated 150 mm dishes and allowed to grow until 70%–80% confluency. Cells were washed with cold PBS and fixed with freshly prepared 4% PFA for 10 min at room temperature with gentle rocking. Crosslinking was quenched by adding 1/10 volume of 1.25 M Glycine for 5 min under the same conditions. After two PBS washes, cells collected and pelleted by centrifugation at 510 × *g* for 5 min at 4°C. The cell pellets were lysed in a buffer containing 50 mM Tris–HCl, pH 7.0, 10 mM ethylenediaminetetraacetic acid (EDTA), 1% SDS, 200 U/ml of RNase inhibitor solution, and 5 µl/ml of proteases inhibitor cocktail. Lysates were sonicated using a Bioruptor (four pulses of 30 s ON and 30 s OFF) to assure complete solubilization. The lysate was centrifuged at 12 000 × *g* for 5 min at 4°C, and the supernatant was collected. An aliquot of the lysate was set aside as the input control. For the pull-down, two 3′-biotinylated NEAT1 probes (AS1: 5′ TGTATCTCTAACCAACCCTCTCCCC/3BioTEG/3′ and AS2: 5′ ACCCTCCCAGCGTTTAGCACACAAT/3BioTEG/3′) were used along with a nonrelated probe (5′ ATAATTTCAAACATCAAATGGTATTTTA/3BioTEG/3′) as a control. Hybridization was carried out using 100 pmol of probe in hybridization buffer (50 mM Tris–HCl, pH 7.0, 750 mM NaCl, 1 mM EDTA, 1% SDS, and 15% formamide) for 4 h on a rotating wheel. Hybridized RNA fragments were captured overnight using streptavidin-coated magnetic beads under rotation. The following day, the beads were washed five times with a 2 × SSC buffer containing 0.5% SDS. RNA–protein complexes were treated with 100 µg of Proteinase K for 45 min at 50°C, followed by incubation at 95°C for 10 min. RNA was separated from the beads using a magnetic rack and purified with 1 ml TRIzol® Reagent (Thermo Fisher Scientific). Purification included phenol extraction, isopropanol precipitation, and DNase treatment, and the RNA was finally resuspended in 20 µl of nuclease-free water. A portion of the extracted RNA was used for cDNA synthesis and RT-qPCR to confirm NEAT1 enrichment. Input samples processed in parallel were used to evaluate pull-down efficiency.

Approximately 100 ng of total RNA from each sample were used for RIP-sequencing. Ribosomal RNA was removed using the Illumina Stranded Total RNA Prep with Ribo-Zero Plus (Illumina). RNA quality and integrity were assessed using an Agilent 2100 Bioanalyzer (Agilent Technologies). Library preparation, sequencing, and bioinformatic analysis were performed by Novogene Co., Ltd. (Cambridge, UK). Libraries were prepared using the NEBNext Ultra RNA Library Prep Kit for Illumina (New England Biolabs) following the manufacturer's protocol. Sequencing was performed on an Illumina NovaSeq X Plus platform, generating ∼12 gigabases of raw data per sample as paired-end 150 bp reads. Sequence quality was assessed with *FASTQC* followed by data trimming. Reads were then aligned to the reference genome using BWA. Duplicates were labeled using *SAMBLAST*, and a mapping quality score threshold of 13 was applied, corresponding to a non-unique region mapping probability of 0.05. Peak calling was performed using MACS2 software (threshold q value = 0.05). Functional enrichment analysis was conducted on all genes associated with *NEAT1*-AS2 probe peaks identified in the RIP-seq data. The analysis was performed using the *clusterProfiler* package in R [46–48].

Neurosphere formation assay

Neurosphere formation was carried out as explained in [30], with some modifications. Briefly, 3000 cells were plated in non-coated flasks with complete medium (EGF and FGF-2) to induce the formation of neurospheres. After 7 days of plating, photos were taken at Leics DM IL LED Fluo microscope (Wetzlar, Germany), and the relative diameter of the spheres was obtained in ImageJ software (v1.53k).

Filopodia density analysis

Immunofluorescence of MAP2 was used to label neurons. Confocal images were taken in Zeiss Confocal Microscope (z = 0.2 µm). The photos were analyzed with ImageJ software, and neurons were reconstructed in NeuronStudio Software (version 0.9.92), as described before [30]. In brief, a three-dimensional dendritic network was constructed using a Sholl analysis through automated segmentation. This network was visualized using spherical representations. Starting from the neuronal soma, concentric circles were drawn outward (covering around ± 100 µm with each circle having a 1 µm interval) along the neuronal projections. This highlighted various neuronal components, with neurites displayed in green, branching indicated by yellow spheres, and spines colored in orange and pink. The soma is shown in red. An assessment of spine density was performed, and the count of spines was determined, based on data obtained from at least 15 neurons for each experimental condition.

Statistical analysis

All experiments were conducted with a minimum of three independent replicates. Graphs and statistical analyses were generated using Graphpad Prism 9. Unless otherwise specified, RT-qPCR data are presented as mean with standard

deviation. Comparative analyses to assess differences between experimental groups utilized Mann–Whitney's U or unpaired samples *t*-tests, along with one-way Analysis of Variance (ANOVA) complemented by a Tukey or Bonferroni *post hoc* test for intergroup comparisons. Statistical significance was determined for values of $P < .05$ (*), $P < .01$ (**), $P < .001$ (***), or $P < .0001$ (****). Gene enrichment analyses from significantly altered genes were provided by BGI or conducted using Enrichr v2.0 software (http://amp.pharm.mssm.edu/Enrichr/) [49] and https://reactome.org/ [50].

Results

NEAT1 is highly dysregulated in mutant MeCP2 models, including human neural cells and samples from RTT patients

Previously, we examined the altered noncoding profile of a human RTT cellular model through bulk analysis of NPCs derived from the ventral mesencephalon (RenCells™), focusing specifically on two types of ncRNAs: circRNAs and T-UCRs [30]. We generated two distinct *MECP2*-KO cell clones, labeled A33 and 3F, both of which disrupt the reading frame and abolish MeCP2 protein production (Supplementary Fig. S1A and see below description of Fig. 3B). To comprehensively investigate the impact of *MECP2* loss during the early stages of neural differentiation with single-cell resolution, we first performed scRNA-seq in the *MECP2*-KO A33 clone to assess the transcriptomic profile of neural progenitors across a time-course of spontaneous (free) differentiation. As anticipated, scRNA-seq analysis of WT and *MECP2*-KO NPCs revealed distinct transcriptomic trajectories when comparing KO and WT cells (Fig. 1A). Confirmation of cell cycle arrest upon initiation of differentiation was observed, with some cells still cycling at days 3 and 7 of *in vitro* differentiation, but the majority of cells transitioning to G1 phase beyond that point (Supplementary Fig. S1B). Dysregulation of transcriptional programs in *MECP2*-KO cells was evidenced by an upregulation of astrocytic signatures (Fig. 1B and Supplementary Fig. S1C), consistent with observed dysregulation of glial function in both RTT patients and models [51].

We next ranked the transcripts exhibiting the most significant dysregulation upon differentiation and identified the lncRNA *NEAT1* as the top downregulated gene when considering all time points (Fig. 1C). This finding was confirmed by an additional scRNA-seq experiment, in which the *MECP2*-KO 3F clone was analyzed alongside the WT and *MECP2*-KO A33 clone during a 7-day differentiation experiment (Supplementary Fig. S1D). Single-cell analysis of differentiating neural progenitors revealed a virtual absence of *NEAT1* in *MECP2*-KO cells throughout the differentiation trajectories (Fig. 1D and Supplementary Fig. S1E). *NEAT1* is a very abundant lncRNA existing as two isoforms within the cell: a shorter 3.7 kb isoform (*NEAT1_1*) and a much longer 23 kb long isoform (*NEAT1_2*), both originating from the same promoter and produced through alternative transcription termination sites (see diagram in Fig. 1E). Downregulation of both *NEAT1* isoforms in *MECP2*-KO clones was confirmed by RT-qPCR in human neural progenitor and differentiated cells (Fig. 1E). Moreover, restoration of MeCP2 levels via ectopic transfection also led to the upregulation of *NEAT1* levels, confirming the causal relationship between MeCP2 loss and *NEAT1* downregulation (Fig. 1F). Additionally, analysis of RTT patient-derived iPS cells harboring the point mutation *MECP2*-T158M and its isogenic control revealed comparable levels of *NEAT1* expression, which were significantly reduced in the mutant cells during differentiation into neural progenitors (Fig. 1G and Supplementary Fig. S1F). These findings suggest dynamic regulation of *NEAT1* by MeCP2 in distinct neural contexts. Given reports of *NEAT1* dysregulation in neurological disorders, particularly neurodegenerative diseases such as Alzheimer's disease and Parkinson's diseases (PD) [52–54], we further validated altered *NEAT1* levels in the hippocampus of post-mortem samples and peripheral blood from patients (Fig. 1H and I). Interestingly, in these mature tissues, *NEAT1* levels were upregulated, contrasting with the downregulation observed in neural progenitors and during early stages of differentiation. This underscores *NEAT1* impairment as a common feature across various RTT models and tissues, with specific manifestations likely influenced by cell type and developmental stage.

NEAT1 expression exhibits significant variability among cells, and its presence correlates with the negative regulation of mTORC1

Analysis of expression during the differentiation of WT cells revealed a decrease in *NEAT1* levels as cells transitioned into neurons (Fig. 2A), consistent with previous findings showing a decline in *NEAT1* expression with neuronal activity [55]. Further, scRNA-seq analysis unveiled considerable heterogeneity in *NEAT1* expression among progenitor cells and within each time point across the differentiation trajectory when compared for example with *MECP2* expression (Fig. 2A). Variance analysis further demonstrated that *NEAT1* ranks 45th among the top 1000 most highly variable genes (highlighted in red) in WT NPCs (Supplementary Fig. S2A, standardized variance = 2.9981). When cells from all differentiation timepoints are considered, NEAT1 ranks 237th (Supplementary Fig. S2B, standardized variance = 2.3847). In contrast, *MECP2* is not among the most highly variable genes (Supplementary Fig. S2A and B).

RNA-FISH confirmed the high variability of *NEAT1* expression among cells in the WT line (Fig. 2B). Prompted by these observations and aiming to elucidate *NEAT1*'s function in neural progenitors at the cellular level, we categorised cells based on *NEAT1* expression levels and identified transcripts exhibiting the highest positive and negative correlation with *NEAT1 (*as depicted in the Volcano plot in Fig. 2C). Cells expressing high levels of *NEAT1* displayed elevated expression of genes involved in catabolic processes and the negative regulation of TOR signaling, including *SESN2*, *SESN3* (which modulate mTORC1 signaling via the GATOR complex), and *DDIT4* (which primarily inhibits mTORC1 signaling by targeting the mTORC1 activator, Rheb) (Fig. 2D). In contrast, cells with low *NEAT1* expression displayed enrichment in transcripts associated with DNA replication and the cell cycle (Fig. 2D). Given the observed reduction in *NEAT1* levels in *MECP2* mutant cells, we hypothesized that similar processes might be disrupted in cellular models of RTT. Intriguingly, bulk transcriptomic analysis of human NPCs bearing a common MeCP2 mutation in RTT (R133C) found enrichment in pathways related to translation (Fig. 2E). Specifically, upregulated genes in cells with the R133C mutation were associated with the positive regulation of TOR signaling (Fig. 2F), contrasting with the findings in cells expressing high levels

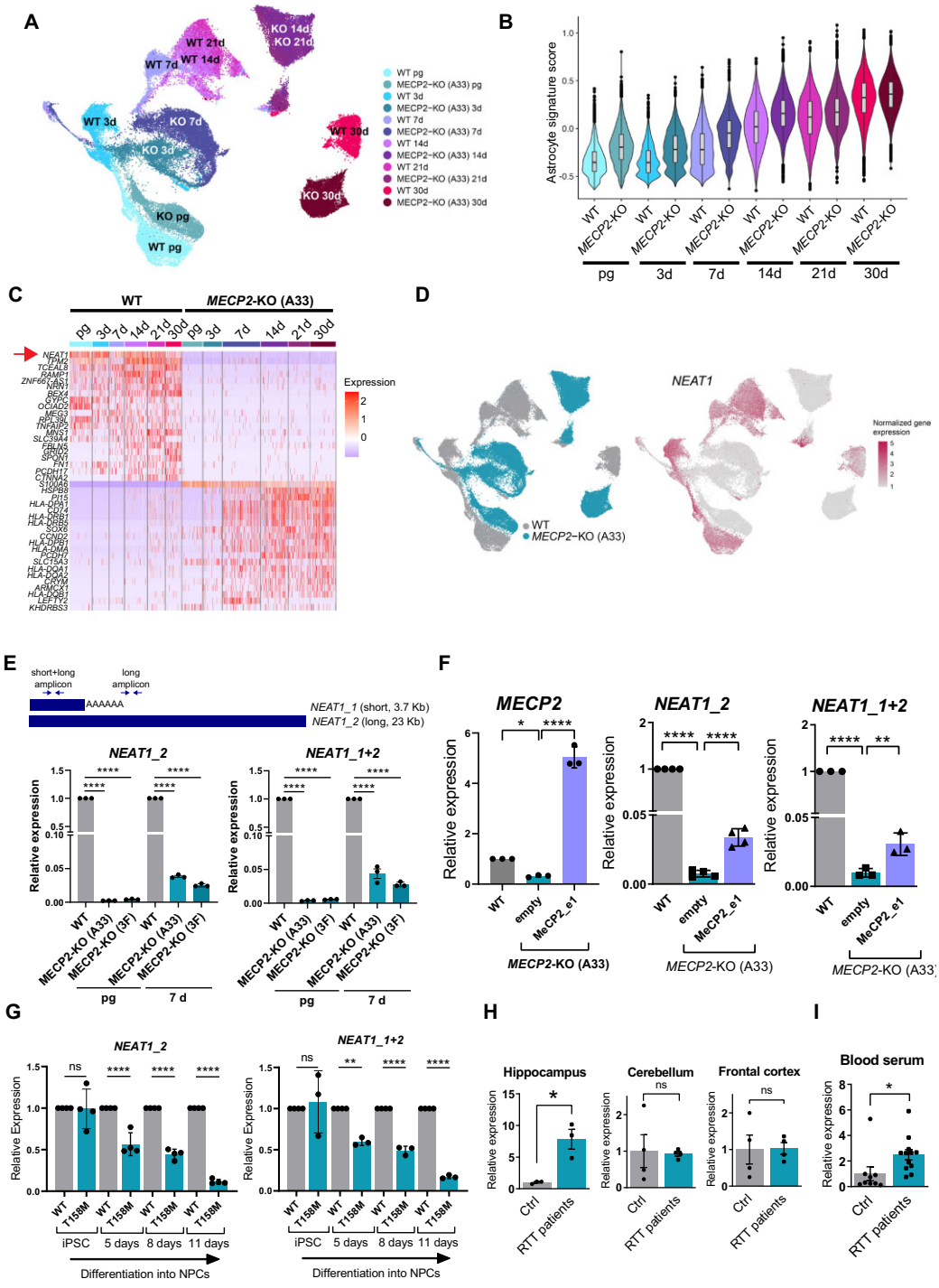

Figure 1. *NEAT1* is highly dysregulated in mutant MeCP2 models, including human neural cells and RTT patient samples. (**A**) UMAP plot of NPCs [WT and *MECP2*-KO (clone A33)] across all timepoints, labeled according to sample. (**B**) Astrocyte signature score across samples. (**C**) Heatmap of the top differentially expressed genes between WT and *MECP2*-KO (clone A33) cells, across all time points. (**D**) (Left) UMAP plot of NPCs (WT and *MECP2*-KO) across all timepoints, labeled according to *MECP2* genotype status; (Right) UMAP plot showing the normalized *NEAT1* expression in all NPCs (WT and *MECP2*-KO). (**E**) Expression levels of *NEAT1* measured by RT-qPCR in WT and *MECP2*-KO progenitor cells (pg) or after 7 days of free differentiation (7 d). Two different *MECP2*-KO clones (A33 and 3F) were analyzed. Primers used are depicted in the upper diagram. *NEAT1_2* signal corresponds to the long isoform, and *NEAT1_1 + 2* signal detects both the short (*NEAT1_1*) and the long (*NEAT1_2*) isoforms. Graphs show the mean ± SD of three replicates (****$P < .0001$, one-way ANOVA). (**F**) Expression levels of *MECP2* and *NEAT1* detected by RT-qPCR in WT, *MECP2*-KO (clone A33) or *MECP2*-KO cells transfected with *MECP2*_e1 construct. Graphs show the mean ± SD of three (*MECP2* and *NEAT1_2* levels) or four (*NEAT1_1 + 2*) replicates (*$P < .05$, **$P < .01$, ****$P < .0001$, one-way ANOVA). (**G**) Expression levels of *NEAT1* in RTT patient-derived iPS cells (T158M and the isogenic WT control) and in the same cells differentiated into neural progenitor cells (NPCs) for the indicated times. Graphs show the mean ± SD of three (*NEAT1_2*) or four (*NEAT1_1 + 2*) replicates (**$P < .01$, ****$P < .0001$, ns = not significant, one-way ANOVA). (**H**) Expression levels of total *NEAT1* (both isoforms) in the hippocampus ($n = 3$), cerebellum ($n = 4$) and frontal cortex (n = 4) of post-mortem RTT patients or healthy control samples. Graphs show the mean ± SEM of replicates (unpaired *t*-test, *$P < .05$, ns = not significant). (**I**) Expression levels of total *NEAT1*in the peripheral blood of $n = 12$ RTT patients. The graph shows the mean ± SEM of replicates (unpaired *t*-test, *$P < .05$). See also Supplementary Fig. S1.

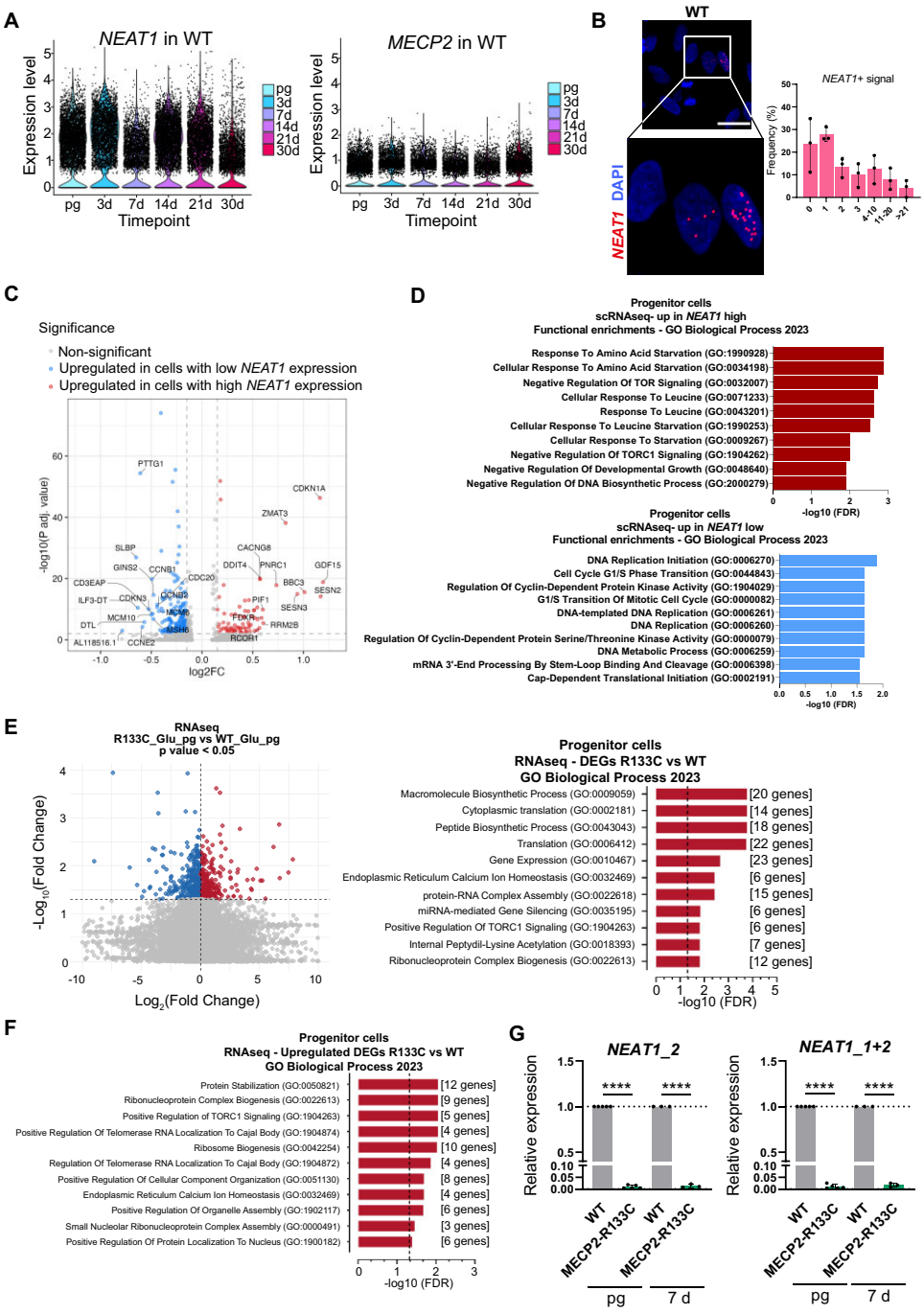

Figure 2. *NEAT1* expression is highly variable between cells and its presence correlates with negative regulation of mTORC1. (**A**) Normalized expression levels for *NEAT1* (left) and *MECP2* (right) across timepoints in single-cell analysis. (**B**) (Left) RNA-FISH showing localization of *NEAT1* in WT NPCs. Scale bar = 20 μm. (Right) Frequency distribution of *NEAT1* RNA-FISH foci per cell. The x-axis represents the number of RNA-FISH foci per cell, and the y-axis indicates the percentage of cells with the corresponding number of foci. Data are represented as the mean ± SD of $n = 50$ WT NPCs in three independent experiments. (**C**) Volcano plot showing differentially expressed genes between progenitor cells with high (>60th percentile of normalized *NEAT1* expression) and low (<60th percentile) *NEAT1* expression. The top differentially expressed genes are highlighted. Dashed lines indicate 0.15 as average $\log_2$ fold change threshold (x axis) and 0.01 as *P* adjusted value threshold (y axis). For clarity, *NEAT1* ($\log_2$FC = 2.4338, *P* adj. value = 0) and *MALAT1* [$\log_2$FC = 0.7312, $-\log_{10}$ (*P* adj. value = 206.68)] are not included in the plot. (**D**) (Above) Enriched Gene Ontology terms for the top 20 upregulated genes in cells with high *NEAT1* expression as identified by functional clustering (Enrichr). The y axis shows the GO terms and the x axis shows the statistical significance (two-tailed Fisher's exact test). (Below) Same as above, for the top 20 genes upregulated in cells with low *NEAT1* expression. (**E**) (Left) Volcano plot showing gene expression changes ($-10 < \log_2$FC < 10) in MECP2-R133C point mutant cells relative to WT progenitor cells. Upregulated genes are shown in red, downregulated genes in blue. The dotted vertical line indicates $\log_2$FC = 0, and the dotted horizontal line represents a *P*-value = .05. (Right) enriched Gene Ontology terms for all differentially expressed genes in R133C cells (*P*-value < .05) as identified by functional clustering (Enrichr). (**F**) Enriched Gene Ontology terms for all upregulated genes in R133C cells (FC > 1, *P*-value < .05) as identified by functional clustering (Enrichr). (**G**) Expression levels of *NEAT1* measured by RT-qPCR in WT and *MECP2*-R133C progenitor cells (pg) or after 7 days of free differentiation (7 d). *NEAT1_2* signal corresponds to the long isoform, and *NEAT1_1 + 2* signal detects both the short (*NEAT1_1*) and the long (*NEAT1_2*) isoforms. Graphs show the mean ± SD of $n = 5$ (pg) or $n = 3$ (7 d) replicates (****$P < .0001$, one-way ANOVA). See also Supplementary Fig. S2.

of *NEAT1*. Notably, these R133C mutant NPCs also exhibited very low levels of *NEAT1* (Fig. 2G). Taken together, our observations suggest functional similarities between *NEAT1* and *MECP2* mutant cells. Subsequently, we aimed to investigate the potential functional involvement of *NEAT1* in the *MECP2* phenotype.

Transcriptomic alterations in *NEAT1*-KO neural cells are similar to those observed in *MECP2*-KO cells

To develop a cellular model suitable for studying *NEAT1*'s role in early neural differentiation, we employed a CRISPR/Cas9 strategy to generate *NEAT1*-KO cells. *NEAT1*-KO NPCs displayed depletion levels of *NEAT1* comparable to those observed in *MECP2*-KO cells (Fig. 3A). Additionally, we established stable cell lines expressing two different shRNAs, which achieved a moderate but significant reduction in *NEAT1* levels (Fig. 3A). Interestingly, *NEAT1* depletion did not result in marked alterations in *MECP2* expression, at either the RNA or protein level (Fig. 3B and Supplementary Fig. S3A), indicating that *NEAT1* acts downstream of *MECP2* and does not regulate *MECP2* levels in human NPCs, contrary to findings in some cancer models [56]. RNA-FISH confirmed the depletion of *NEAT1* expression in *NEAT1*-KO cells, reducing levels to those observed in *MECP2*-KO cells (Fig. 3C). The functional impact of *NEAT1* depletion was further validated through the analysis of α-synuclein levels (SNCA), a known target of *NEAT1* [57, 58]. *SNCA* levels were diminished in *MECP2*-KO, *NEAT1*-KO, and *NEAT1*-shRNA cells (Supplementary Fig. S3B) and were upregulated upon MeCP2 overexpression, demonstrating a positive correlation with *NEAT1 levels* (Supplementary Fig. S3C). In contrast, the expression of *MALAT1*, another highly abundant ncRNA that localizes to nuclear speckles and is located 50 kb downstream of the *NEAT1* locus, remained unaltered following genomic edition of the *NEAT1* promoter (Supplementary Fig. S3D and S3E, as shown by both RNA-FISH and RT-qPCR approaches).

Remarkably, bulk RNA-seq analysis of WT, *MECP2*-KO, and *NEAT1*-KO cells revealed a significant overlap in the dysregulated genes when comparing *MECP2*-KO and *NEAT1*-KO neural progenitor or freely differentiated cells to the WT condition (Fig. 3D). Specifically, 53% of DETs in *MECP2*-KO progenitor cells (1770 out of 3332) and 47% in *MECP2*-KO 7 days differentiated cells (2307 out of 4944) were also dysregulated in *NEAT1*-KO cells, indicating that the absence of *NEAT1* contributes significantly to the *MECP2*-KO phenotype, particularly in this cellular context (Supplementary Fig. S3F). These percentages remained consistent when analyzing upregulated and downregulated transcripts separately (Supplementary Fig. S3G and S3H). KEGG enrichment analysis of the dysregulated genes in *NEAT1*-KO cells highlights the impact of *NEAT1* loss on neurological diseases, including PD, Huntington's disease, and other neurodegenerative disorders, underscoring the crucial role of *NEAT1* in neural function (Fig. 3E), as previously reported [59, 60].

The downregulation of *NEAT1* in *MECP2*-KO cells impacts protein metabolism, vesicle trafficking, and mitochondrial function in human neural cells

To gain insight into the potential effects of *NEAT1* deficiency on the mTOR pathway and protein metabolism, as suggested by transcriptomic and enrichment analysis, we examined the levels of key members of the pathway. DDIT4, which positively correlated with *NEAT1* expression in our scRNA-seq analysis (Fig. 2C), serves as a crucial mediator of the cellular stress response by inhibiting mTORC1 activity. Additionally, in neurons, DDIT4 is required for normal neuronal migration during embryonic brain development [61]. Western blot analysis revealed aberrantly low levels of DDIT4 protein in both *MECP2*-KO and *NEAT1*-KO NPCs (Fig. 4A). Simultaneously, activation of ribosomal protein S6, which triggers protein translation initiation and whose phosphorylation serves as a readout for mTORC1 activity and protein synthesis, was significantly increased in both mutant cell types, despite a mild decrease in total mTOR levels (Fig. 4B). An abnormal increase of mTOR-S6K signaling has previously been observed in RTT patients [62], although the molecular mechanisms underlying this phenomenon remain unclear. Importantly, ectopic expression of the full-length *NEAT1_2* isoform (22 kb) in *MECP2*-KO cells restored S6 inhibition (Fig. 4B and Supplementary Fig. S4A–C), indicating that *NEAT1* plays a pivotal role in mTOR pathway inhibition and that *NEAT1* downregulation may lead to an aberrant increase in protein synthesis. Elevated levels of protein synthesis can sometimes result in the presence of aberrant protein aggregates within the cell and were evidenced by ProteoStat® staining in both *MECP2*-KO and *NEAT1*-KO or *NEAT1*-shRNA cells (Fig. 4C). To further corroborate the importance of *NEAT1* absence in driving protein aggregation in *MECP2*-KO cells, we employed the CRISPR/SAM approach to reactivate endogenous gene expression [41, 63]. The CRISPR/SAM system utilizes a catalytically inactive Cas9 (dCas9) fused to a transcriptional activator domain (such as VP64) to precisely target specific genomic loci and upregulate gene expression through recruitment of transcriptional machinery. To this end, we tested several *NEAT1*-specific sgRNAs (Supplementary Fig. S4D and E). Using three different sgRNAs directed at the *NEAT1* promoter, we observed a decrease in protein aggregation levels in *MECP2*-KO cells, confirming *NEAT1* defects as the underlying cause of aberrant protein aggregation in these cells (Fig. 4D).

Using these tools, we compared the ultrastructural features of WT NPCs with those of *MECP2*-KO and *NEAT1*-KO cells. All KO cells displayed multiple defects, including mitochondria with high electron density matrices, indicative of hyperactivity, as well as an abnormally high number of vesicles, including endosomal and autophagosomal structures. Notably, autophagosomes with multilamellar membranes were observed forming and fusing with mitochondria organelles (yellow arrows), ultimately leading to mitophagy (Fig. 4E and Supplementary Fig S5A). This suggests a potential overload of mitochondria and/or a slow or defective autophagic process. Consistent with this, a previous study in blood cells from RTT patients had proposed that mitochondria are not properly eliminated in RTT due to autophagy defects [64]. Abnormal mitochondrial function was further confirmed by a Mito-SOX-based assay and flow cytometric analysis, which detects mitochondrial reactive oxygen species (ROS). RTT cells are known for increased ROS levels [65, 66], and interestingly, while *MECP2*-KO and *NEAT1*-KO cells showed a similar mitochondrial mass staining (MitoTracker, Fig. 4F, and AIF measurement, Supplementary Fig. S5B and C), we detected increased ROS levels compared to control cells (Fig. 4G). Instead, mitochondrial activity appeared impaired, as

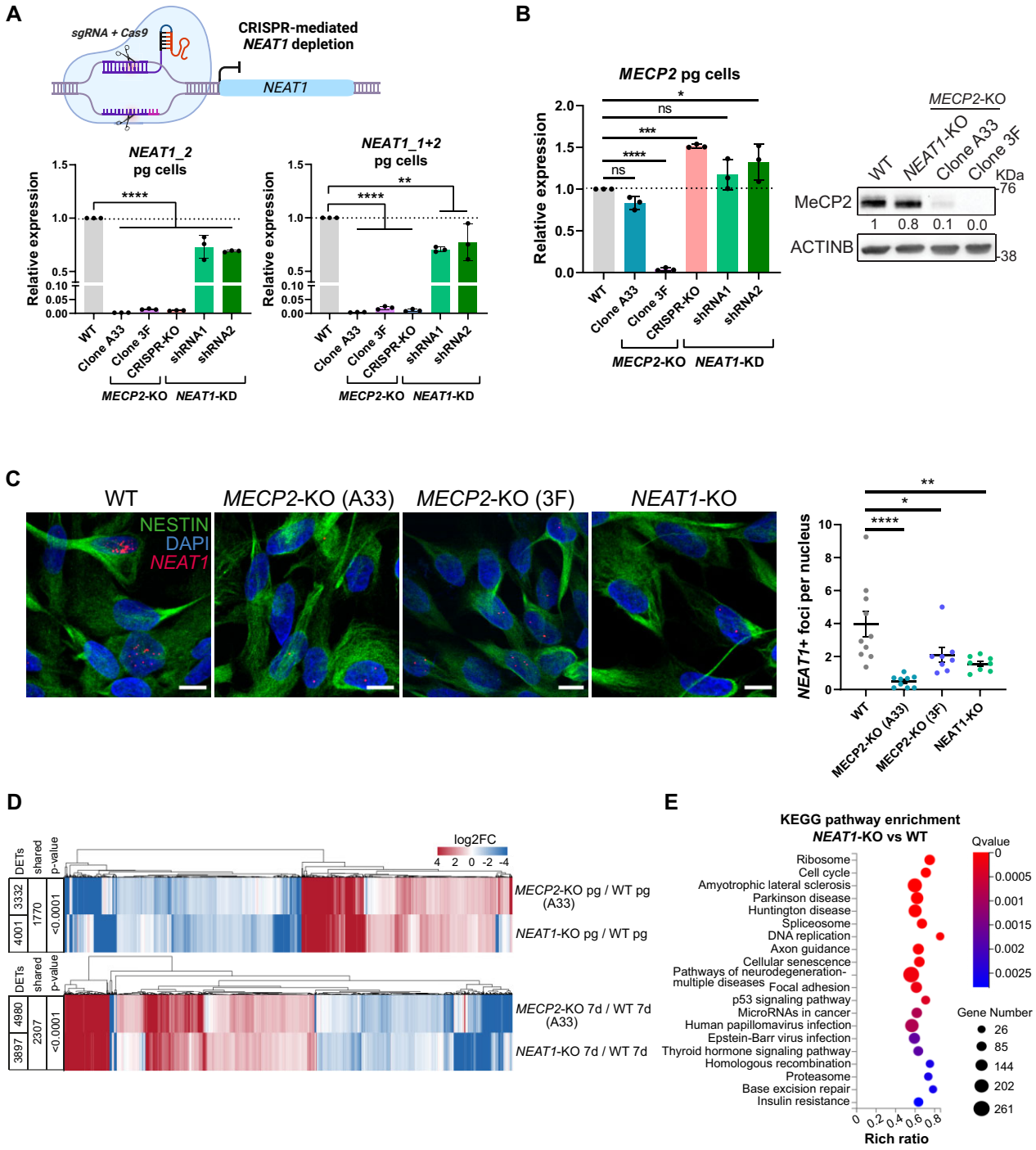

Figure 3. *NEAT1*-KO neural cells display transcriptomic alterations similar to *MECP2*-KO cells. (**A**) *NEAT1* depletion levels in *MECP2*-KO (clones A33 and 3F), *NEAT1*-KO cells edited by CRISPR/Cas9, and in *NEAT1* shRNA-depleted cells were assessed by RT-qPCR. Graphs show the mean ± SD of three replicates (***P* < .01, *****P* < .0001, one-way ANOVA). Diagram was created in BioRender. Soler (2025) https://BioRender.com/o10b971. (**B**) (Left) *MECP2* mRNA levels measured by RT-qPCR. Graph shows the mean ± SD of three replicates (**P* < .05, ****P* < .001, *****P* < .0001, ns = not significant, one-way ANOVA). (Right) Western blot analysis of MeCP2 in WT or KO progenitor cells. Quantification of band intensity is shown below each lane. (**C**) (Left) RNA-FISH showing abundance of *NEAT1* in WT, *MECP2*-KO (clones A33 and 3F) or *NEAT1*-KO NPCs. Scale bar = 10 μm. (Right) Quantification of *NEAT1* presence per cell nucleus. Graph represents the mean ± SEM of the number of nuclear *NEAT1* + foci in *n* = 9 cells (**P* < .05, ***P* < .01, *****P* < .0001, one-way ANOVA). (**D**) Heatmaps of differentially expressed transcripts (DETs) ($|\log_2 FC| \geq 1$, q value ≤ 0.05) in *NEAT1*-KO and *MECP2*-KO (clone A33) NPCs (top) and 7-day differentiated cells (bottom) relative to WT cells. The number of condition-specific or shared DETs is shown to the left of the heatmaps together with the *P*-value from the hypergeometric test for the overlap between the conditions. (**E**) Enriched KEGG pathways for all differentially expressed genes (q value ≤ 0.05) in *NEAT1*-KO NPCs relative to WT cells, as identified by functional clustering (Enrichr). See also Supplementary Fig. S3.

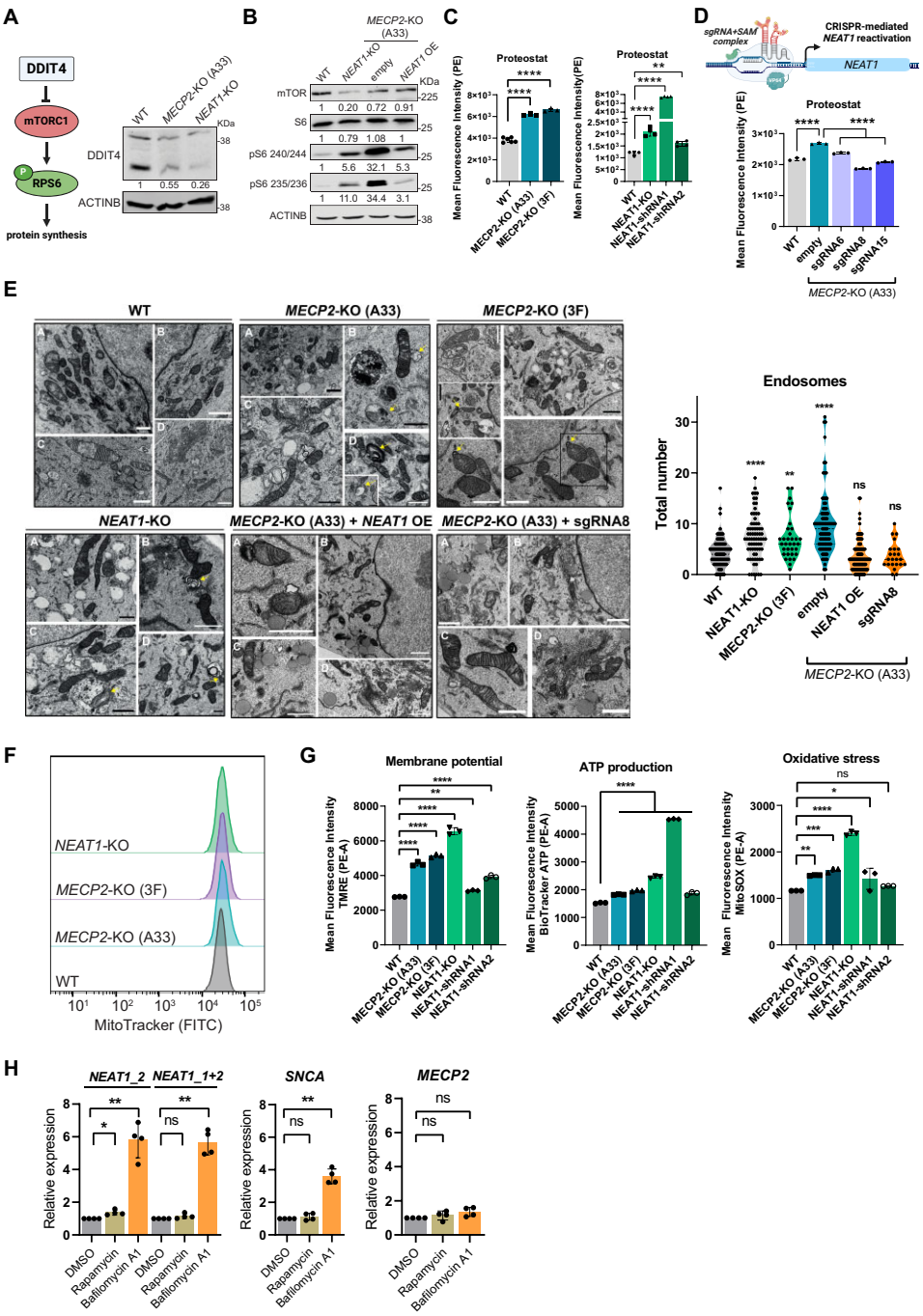

Figure 4. *NEAT1* downregulation in *MECP2*-KO cells impacts protein metabolism, vesicle trafficking and mitochondrial function of human neural cells. (**A**) Western blot analysis of DDIT4 levels in *MECP2*-KO (clone A33) and *NEAT1*-KO progenitor cells. Diagram was created in BioRender. Soler (2025) https://BioRender.com/i12q588. (**B**) Western blot analysis of mTOR, total S6 and phosphorylated-S6 levels in *NEAT1*-KO, *MECP2*-KO and *MECP2*-KO overexpressing *NEAT1* progenitor cells. Quantification of band intensity is shown below each lane. (**C**) (Left) Assessment of protein aggregation in WT or *MECP2*-KO (clones A33 and 3F) NPCs with ProteoStat® dye. Graph shows the mean ± SD of three replicates (****$P < .0001$, one-way ANOVA). (Right) Same assay in *NEAT1*-KO or *NEAT1*-shRNA depleted cells. Graph shows the mean ± SD of four replicates (**$P < .01$, ****$P < .0001$, one-way ANOVA). (**D**) Protein aggregation quantified with ProteoStat® dye in WT, *MECP2*-KO (clone A33) cells (empty) or *MECP2*-KO cells with *NEAT1* reactivation with three different sgRNAs. The graph shows the mean ± SD of three replicates (****$P < .0001$, one-way ANOVA). Diagram was created in BioRender. Soler (2025) https://BioRender.com/r99k484. (**E**) (Left) Representative transmission electron micrographs of WT, *MECP2*-KO (clones A33 and 3F), *NEAT1*-KO or *MECP2*-KO (A33) with *NEAT1_2* overexpression or reactivation by means of CRISPRa (sgRNA8) progenitor cells. Mitophagy is indicated by arrows. Scale bars = 1 μm. (Right) Quantification of the number of endosomes in the same conditions. $n = 30$ micrographs, (**$P < .01$, ****$P < .0001$, ns = not significant, one-way ANOVA). (**F**) Histogram overlay of MitoTracker™ intensity (FITC detection) to compare mitochondria presence in WT, *MECP2*-KO (clones A33 and 3F) and *NEAT1*-KO NPCs. (**G**) Graphs of the mean fluorescence intensity of TMRE (membrane potential), ATP Tracker (ATP production), and MitoSOX (oxidative stress) measured by the PE-A filter, normalized with FITC-A detection of MitoTracker™. Graphs show the mean ± SD of three replicates (ns = not significant, *$P < .05$, **$P < .01$, ***$P < .001$, ****$P < .0001$, one-way ANOVA). (**H**) Expression levels of *NEAT1*, *SNCA* and *MECP2* mRNAs were analyzed by RT-qPCR in NPCs treated with the indicated compounds. Graphs represent the mean ± SD of four independent replicas (ns = not significant, *$P < .05$, **$P < .01$, one-way ANOVA). See also Supplementary Figs S4 and S5.

indicated by similar alterations in mitochondrial membrane potential and ATP production observed in *MECP2*-KO, *NEAT1*-KO, and *NEAT1*-shRNA cells (Fig. 4G). This finding corroborates the hyperactivity suggested by ultrastructure imaging (Fig. 4E). Taken together, these results suggest that *NEAT1* downregulation following MeCP2 loss of function may contribute to mitochondrial abnormalities and the disruption of mitochondrial homeostasis in RTT.

The presence of abnormal protein accumulation, a higher number of vesicles, and mitochondrial impairment strongly suggest a significant involvement of *NEAT1* in protein metabolism and related pathways. Therefore, we next investigated whether commonly used inhibitors of the mTOR and autophagy processes affected *NEAT1* levels in WT cells. Treatment with the mTOR inhibitor Rapamycin, at levels sufficient to induce S6 dephosphorylation (Supplementary Fig. S5D), did not significantly alter lysosomal or autophagic gene expression and only had a marginal impact on *NEAT1* levels (Supplementary Fig. S5E and Fig. 4H). In contrast, treatment with BafilomycinA1, which impedes lysosomal acidification and blocks autophagic flux, leading to the accumulation of autophagosomes in the cell, resulted in enhanced LC3-II protein levels as expected (Supplementary Fig. S5D). Notably, it also induced a sharp increase in *NEAT1* levels, along with elevated levels of its downstream target *SNCA* (Fig. 4H). Conversely, *MECP2* expression levels remained unaltered in response to both compounds. These findings suggest that *NEAT1* functions in response to altered autophagic dynamics and further confirm the role of this lncRNA in essential cellular processes in NPCs.

Given that *NEAT1* is upregulated in response to deficits in autophagic flux and considering the close relationship between autophagy and mitochondrial function in maintaining cellular homeostasis, energy balance, and overall cell health, we proceeded to compare the responses of cells to these same inhibitors when *NEAT1* is absent (*MECP2*-KO and *NEAT1*-KO cells) by measuring key readouts of mitochondrial function. Compared to WT cells, treatment with BafilomycinA1 failed to elicit changes in oxidative stress-related processes in either *MECP2*-KO or *NEAT1*-KO cells, as indicated by the MitoSOX assay (Supplementary Fig. S5F). Similarly, ATP production increased only in WT cells but not in *MECP2*-KO or *NEAT1*-KO cells (Supplementary Fig. S5G). In contrast, the membrane potential (measured using TMRE) remained unchanged under all conditions (Supplementary Fig. S5H). Overall, these findings suggest that the downregulation of *NEAT1* as a consequence of *MECP2* mutation hinders the cellular response to autophagy inhibitors, underscoring the importance of *NEAT1* in maintaining mitochondrial function and cellular homeostasis.

Next, we aimed to explore the molecular mechanisms underlying *NEAT1*'s involvement in autophagy and how this process is compromised in *MECP2* mutant cells.

Reactivation of *NEAT1* in *MECP2*-KO cells restores the levels of autophagy-related proteins

To gain more insight into the status of autophagic flux in the mutant cells, we employed a mCherry-GFP-LC3 reporter to visualize vesicle maturation trafficking, enabling the differentiation between autophagosomes and autolysosomes [43]. Autophagosomes exhibit both GFP and mCherry fluorescence, producing a green and yellow signal, while autolysosomes are labeled red due to the inability of GFP to maintain its native conformation in the acidic lysosomal environment (Fig. 5A). Following 16 h of autophagy induction, both *MECP2* and *NEAT1*-KO cells exhibit a similar increase in the ratio of autolysosomes to autophagosomes compared to WT cells (Fig. 5B), validating abnormal dynamics of the autophagic flux in the mutant cells and implying that the defects in *MECP2*-KO cells result from *NEAT1* downregulation. Analysis of lysosomal markers LAMP1 and LAMP2 (integral membrane glycoproteins primarily localized to the lysosome and late endosome membranes) further confirmed abnormal accumulation in *MECP2*-KO cells, both at the progenitor stage and during differentiation (Fig. 5C), which could be reversed by ectopic overexpression of MeCP2 protein (Fig. 5D). Interestingly, similar LAMP1 accumulation was observed in *NEAT1*-KO and *NEAT1*-shRNA cells, as evidenced by both western blot and immunofluorescence assays (Fig. 5E and F).

Accumulation of autolysosomes and other undegraded autophagic structures can result from various defects, including deficiencies in cargo sequestration into autophagosomes, impairment in autophagosome formation, and improper fusion with lysosomes. Autophagy-related (ATG) proteins play crucial roles in all these stages of the autophagy process, encompassing autophagosome assembly, cargo recognition, and fusion with lysosomes, all of which may contribute to autolysosome accumulation. Therefore, we next investigated ATG protein levels following *MECP2* KO. As shown in Fig. 5G, several ATG proteins, including ATG3, ATG16L1, ATG16L2, ATG12-ATG5, and Beclin-1/ATG6, were decreased in *MECP2*-KO cells, with a minor reduction observed for ATG7. Overexpression of MeCP2 restored these deficits (Fig. 5G), confirming the role of MeCP2 in regulating ATG family protein levels. However, these protein-level changes did not correlate with changes in the respective mRNAs, which were largely unaffected by either MeCP2 downregulation or overexpression, except for *ATG16L1* mRNA, which was significantly upregulated in *MECP2*-KO clones (Fig. 5H). These findings suggest that MeCP2 regulates ATG proteins through mechanisms beyond transcriptional control.

To evaluate the contribution of *NEAT1* in the downregulation of ATG proteins, we examined protein and mRNA levels in *NEAT1*-depleted cells. Remarkably similar to *MECP2*-KO cells, a pronounced reduction in protein levels was observed for ATG3, ATG16L1, ATG16L2, ATG12-ATG5, and Beclin-1, with less evident changes for ATG7 (Fig. 5I). Interestingly, mRNA levels remained unaltered (Supplementary Fig. S6A), indicating that similar regulatory mechanisms are at play in both *MECP2*- and *NEAT1*-mutant lines. Examination of RNA-seq data from WT, *MECP2*-KO, and *NEAT1*-KO cells also revealed no decrease in the mRNA levels of autophagy genes (Supplementary Fig. S6B). Crucially, reactivation of *NEAT1* in *MECP2*-KO cells using CRISPR/SAM with different sgRNAs successfully restored deficits in ATG protein levels, again independently of mRNA levels (Fig. 5J and K). Furthermore, overexpression of *NEAT1*, but not *MALAT1* (used as a control), rescued ATG protein levels in *NEAT1*-KO cells (Fig. 5L and Supplementary Fig. S6C). Altogether, these findings confirm *NEAT1* as the primary mediator of MeCP2 regulation of autophagy-related genes and the principal contributor to impaired autophagic flux in *MECP2*-KO neural cells.

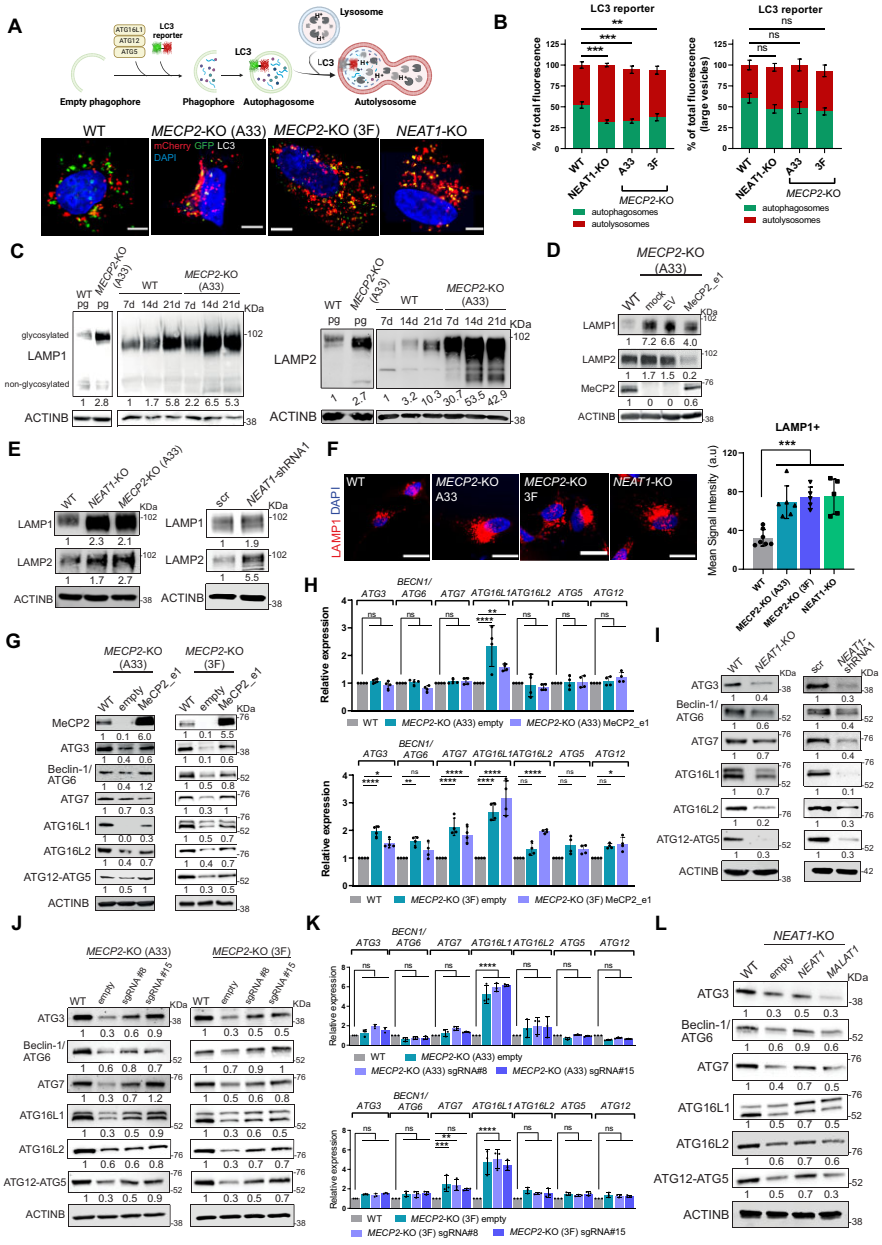

Figure 5. *NEAT1* reactivation in *MECP2*-KO cells rescues the levels of autophagy-related family of proteins. (**A**) Top diagram: Autophagic vesicle maturation can be monitored in cells expressing the mCherry-GFP-LC3 reporter, which is sensitive to the increased acidic conditions in autolysosomes relative to autophagosomes. Concomitant expression of GFP- and mCherry-fused LC3 in autophagosomes is visualized as yellow–green, whereas only the expression of mCherry is allowed by acidic lysosomes and thus autolysosomes are visualized as red fluorescence. Bottom: representative images of WT, *MECP2*-KO (clones A33 and 3F) and *NEAT1*-KO NPCs transfected with the mCherry-GFP-LC3 reporter after autophagy induction (through mTOR inhibition) by administration of Rapamycin (50 μM) for 16 h. Diagram was created in BioRender. Soler (2025) https://BioRender.com/z98e924. (**B**) Quantification of the number of autophagosomes and autolysosomes in WT, *MECP2*-KO (clones A33 and 3F) and *NEAT1*-KO cells ($n \geq 12$ cells per condition, $^{**}P < .01$, $^{***}P < .001$, ns = not significant, one-way ANOVA). (**C**) Western blot analysis of lysosomal markers LAMP1 (left) or LAMP2 (right) levels in WT or *MECP2*-KO cells (clone A33) at the progenitor stage or upon free differentiation (times are indicated). (**D**) Western blot analysis of lysosomal markers LAMP1 and LAMP2 in WT or *MECP2*-KO (clone A33) NPCs, or upon transfection of MeCP2_e1 isoform. MeCP2 levels are also blotted for reference. (**E**) (Left) LAMP1 and LAMP2 levels assessed by western blot in WT, *NEAT1*-KO or *MECP2*-KO (clone A33) cells. (Right) LAMP1 and LAMP2 levels assessed by western blot in control and *NEAT1*-shRNA1 depleted cells. (**F**) (Left) LAMP1 levels assessed by immunofluorescence in WT, *MECP2*-KO (clones A33 and 3F) or *NEAT1*-KO NPCs. (Right) Quantification of the LAMP1 immunofluorescence signal, where the graph represents the mean ± SD of $n = 6$ images ($^{***}P < .001$, one-way ANOVA) (**G**) Western blot analysis of autophagy-related proteins in WT or *MECP2*-KO (clones A33, left, and 3F, right) NPCs transfected with empty vector or MeCP2_e1 isoform. MeCP2 levels are also blotted for reference. (**H**) RT-qPCR analysis of the mRNA of the same genes shown in (**G**). Graphs represent the mean ± SD of four independent replicas ($^{*}P < .05$, $^{**}P < .01$, $^{****}P < .0001$, ns = not significant). (**I**) Western blot analysis of autophagy-related proteins in WT or *NEAT1*-KO (left), or in *NEAT1*-shRNA1 depleted (right) NPCs. (**J**) Western blot analysis of autophagy-related proteins in WT or *MECP2*-KO (clones A33, left, and 3F, right) NPCs transfected with empty vector or two different sgRNAs to reactivate *NEAT1* expression. (**K**) RT-qPCR analysis of the mRNA of autophagy-related genes shown in (**J**). Graphs represent the mean ± SD of three independent replicates ($^{**}P < .01$, $^{***}P < .001$, $^{****}P < .0001$, ns = not significant). (**L**) Western blot analysis of autophagy-related proteins in WT or *NEAT1*-KO NPCs transfected with empty vector, *NEAT1_2* or *MALAT1* vectors. Quantification of band intensity is shown below each western blot lane. See also Supplementary Fig. S6.

NEAT1 interacts with mRNAs of autophagy genes and promotes their nuclear retention

Considering the observed impact on the autophagy process following the loss of *NEAT1* and the unaltered steady-state levels of ATG gene mRNAs (Fig. 5), we investigated their subcellular localization. Previous studies have suggested that one important paraspeckles/*NEAT1* function is to retain certain mRNAs encoding mitochondrial protein components (mito-mRNAs) in the nucleus [67]. In addition, direct RNA targets of *NEAT1* have been reported to preferentially bind to the 5′ end of *NEAT1* [45]; however, the scope and specific mRNAs subject to such regulation remain unclear. To investigate *NEAT1*'s potential role in regulating ATG protein expression via mRNA metabolism, we performed a RIP-seq experiment in WT NPCs. Cells were crosslinked, and endogenous *NEAT1* was pulled down using antisense probes targeting the 5′ (common) region of *NEAT1* isoforms. Associated RNAs were then purified and analyzed by RT-qPCR. The *NEAT1*-AS2 probe effectively retrieved endogenous *NEAT1*, recovering ∼7% of the total *NEAT1* RNA, while the *NEAT1-AS1* probe showed no significant *NEAT1* retrieval (Fig. 6A and Supplementary Fig. S7A). Subsequently, RIP-seq analysis of RNAs from *NEAT1*-AS2 pull-down and control experiments (performed in triplicates) identified enriched transcripts. Gene ontology analysis of the bound transcripts revealed enrichment for categories such as mRNA processing, splicing, and transport, consistent with previous reports [45], along with other processes like ubiquitin-mediated proteolysis, autophagy, and endocytosis (Fig. 6B). Notably, among autophagy-related transcripts, *ATG16L2* exhibited a distinct RIP-seq peak signal with the *NEAT1*-AS2 probe (Fig. 6C), whereas other ATG transcripts showed no specific enrichment (Supplementary Fig. S7B). Further, *in silico* predictions of direct RNA–RNA interactions using IntaRNA [68–71] (http://rna.informatik.uni-freiburg.de/IntaRNA/) suggested energetically stable base-pairing (−28.8 kcal/mol) between the canonical *ATG16L2* transcript (NM_033388.2) and a region within *NEAT1* near the *NEAT1*-AS2 probe (positions 192–242 of *ATG16L2* mRNA; Fig. 6D). RT-qPCR confirmed that this region near the 5′UTR of *ATG16L2* mRNA was enriched in the *NEAT1* pull-down, with ∼3% of input *ATG16L2* mRNA recovered. Given that only ∼7% of *NEAT1* was retrieved, this suggests a significant interaction between *ATG16L2* mRNA and *NEAT1*. None of the other tested ATG mRNAs were present in the pull-down with comparable enrichments, except for one *ATG5* isoform (NM_001286106.2), whose 5′UTR was also enriched in the pull-down (Fig. 6E). Predicted base-pairing interactions between *NEAT1* and this specific *ATG5* region were also energetically stable (Supplementary Fig. S7C). These findings suggest that *NEAT1* selectively interacts with autophagy-related mRNAs, particularly *ATG16L2,* and, to a lesser extent, a specific *ATG5* isoform, likely through direct RNA–RNA interactions.

Since *NEAT1* is able to dictate target RNA localization, RNA *in situ* hybridization assays were next conducted to visualize the localization of *ATG16L2* mRNA in NPCs (Fig. 6F). In WT cells, this mRNA was abundantly detected in the nucleus, whereas in *MECP2*-KO or *NEAT1*-KO cells, it was frequently found in the cytoplasm. Notably, overexpression of the long *NEAT1* isoform (*NEAT1_2*) in *MECP2*-KO cells restored nuclear retention (Fig. 6F). Intriguingly, although not detected in the pull-down assay, RNA-FISH experiments revealed a similar pattern for *ATG16L1*: the mRNA was localized to the nucleus in WT cells, often overlapping with *NEAT1* signal, while both *MECP2*-KO and *NEAT1*-KO cells exhibited a more abundant cytoplasmic signal, which could be partially reverted by overexpression of *NEAT1* (Supplementary Fig. S7D).

To quantitatively assess the effect on mRNA localization, we conducted biochemical cellular fractionation, revealing that *ATG5*, *ATG16L1* and *2*, and *BECLIN/ATG6* mRNAs were abundantly localized in the nucleus of WT NPCs, with *ATG16L2* mRNA displaying particularly striking nuclear enrichment (up to 90%). This nuclear localization in WT cells may serve as a rapid response mechanism for increased protein production during physiological stress. Interestingly, both *NEAT1*-KO and *MECP2*-KO cells showed significantly lower nuclear levels of these mRNAs. Similar patterns were observed for the mito-mRNAs *CPT1A* and *SMURF1* [67], while the localization of *MALAT1* or *GAPDH* remained unaltered in *MECP2*-mutant cells (Fig. 6G and Supplementary Fig. S7E). When considering the impact of this relocation relative to the amount of nuclear mRNA in WT cells, we observed that up to 20% of nuclear mRNA for *ATG* genes was redistributed to the cytoplasm in *MECP2*-KO cells. For comparison, 25% and 30% of nuclear *CPT1A* and *SMURF1* mito-mRNAs, respectively, were relocated (Supplementary Fig. S7F). Importantly, CRISPR-mediated reactivation of *NEAT1* using two different sgRNAs in *MECP2*-KO cells restored the nuclear levels of all mRNAs to those of WT cells (Fig. 6G and Supplementary Fig. S7F). The impact of *NEAT1* downregulation on mRNA localization was specific, as the localization of other ATG mRNAs, such as *ATG3*, *ATG4B*, *ATG7*, *ATG12*, and *ATG13*, remained unaltered, as did *LAMP1/2* mRNAs and other mito-mRNAs (Supplementary Fig. S7G). Overall, this suggests that the specific nuclear retention of ATG mRNAs may not be limited to transcripts interacting with *NEAT1*, even though this lncRNA appears to regulate the nuclear-to-cytoplasmic localization of many ATG mRNAs. It is noteworthy that WT cells display higher nuclear levels of ATG mRNAs than *MECP2*-KO or *NEAT1*-KO cells, while the corresponding proteins are present at lower levels in both KO cells. This counterintuitive finding illustrates how the correct trafficking trajectory and nuclear history of an mRNA may impact its subsequent translation and protein level.

Overall, these findings indicate that the downregulation of *NEAT1* plays a significant role in the dysfunction of the autophagic process observed in *MECP2*-KO cells. The abnormal accumulation of autolysosomes may result from impaired ATG expression and autophagic complex biogenesis, potentially leading to the accumulation of misfolded proteins and damaged organelles, as observed in our ultrastructural analysis.

Re-expression of *NEAT1* reverses the morphological defects of *MECP2*-KO neurons

Given the fundamental roles of autophagy and mitochondrial function in cellular homeostasis, the impact of *NEAT1* on these processes in the context of *MECP2* loss of function suggests a broader contribution of *NEAT1* to the RTT phenotype. Therefore, we further investigated how *NEAT1* contributes to the morphological phenotypes of *MECP2*-KO cells. We and others have previously described that neurosphere for-

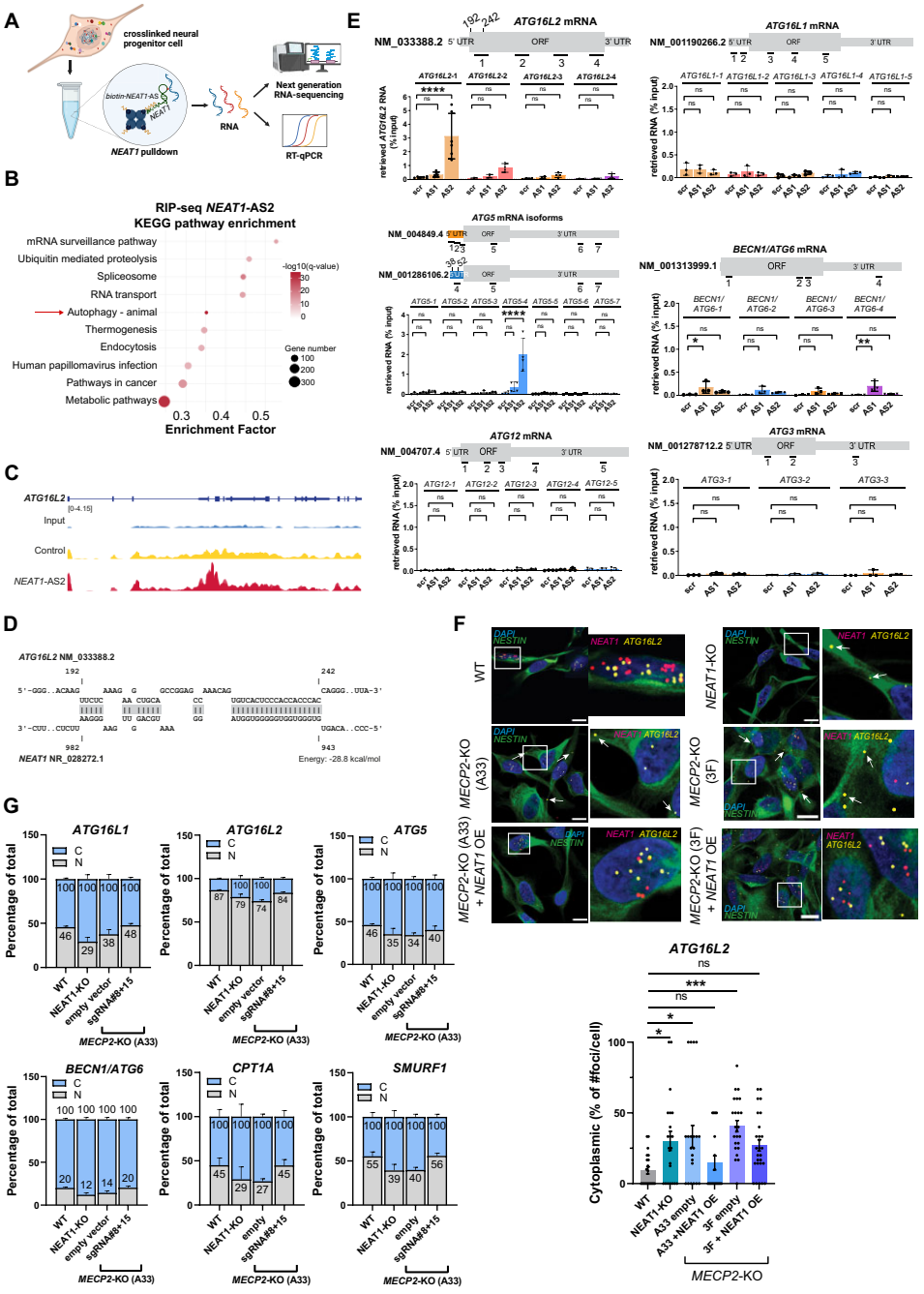

Figure 6. *NEAT1* directly interacts with mRNAs of autophagy-related genes and promotes their nuclear retention. (**A**) Diagram summarizing the strategy for the *NEAT1* pulldown experiment. Cells were crosslinked and endogenous *NEAT1* was retrieved with biotinylated, antisense probes. RNAs bound to *NEAT1* were amplified by next-generation sequencing or RT-qPCR analysis. Diagram was created in BioRender. Soler (2025) https://BioRender.com/w62q250. (**B**) Top 10 enriched functional categories for *NEAT1*-AS2 probe peak-related genes (threshold q value = 0.05) from RIP-seq analysis. (**C**) RIP-seq peak signal profiles across *ATG16L2* (GRCh38/hg38 chr11:72 814 411–72 829 635). (**D**) Predicted interaction between *ATG16L2* (transcript NM_033388.2) with *NEAT1* in the 500 nt region flanking the AS2 probe. The interaction was predicted using IntaRNA (http://rna.informatik.uni-freiburg.de/IntaRNA/) with default parameters, including a minimum seed length of 7 nucleotides. (**E**) RIP-qPCR analysis of the indicated autophagy-related genes. For each transcript, several amplicons were tested, whose locations are indicated above each graph. The graphs represent the mean ± SD of three independent experiments. The enrichments are normalized by the input material and shown relative to scramble (scr) probe. One-way ANOVA test was used, $*P < .05$, $**P < .01$, $****P < .0001$, ns = not significant. (**F**) (Above) RNA-FISH showing localization of *NEAT1* and *ATG16L2* mRNAs in WT, *NEAT1*-KO, *MECP2*-KO (clones A33 and 3F) or *MECP2*-KO clones overexpressing full-length *NEAT1_2* progenitor cells. NESTIN antibody and DAPI staining were used at the same time to visualize the cells. For each cell condition, the white-squared inset is amplified on the right panel. White arrows indicate cytoplasmic signals. Scale bars = 10 μm. (Below) Quantification of *ATG16L2* RNA-FISH signal. Total number of foci were counted in each cell and the percentage of cytoplasmic foci per cell is represented. Graphs show the mean ± SEM of $n \geq 18$ cells ($*P < .05$, $***P < .001$, ns = not significant, one-way ANOVA). (**G**) RT-qPCR assessment of the nuclear-cytoplasmic distribution of the indicated autophagy-related and mitochondrial protein-encoding mRNAs. Biochemical fractionation was done in WT, *NEAT1*-KO and *MECP2*-KO (clone A33) cells transfected with empty or sgRNAs to reactivate *NEAT1*. Percentage of the mRNA present in each fraction relative to total mRNA is shown. Graphs represent the mean ± SD of four independent replicas. See also Supplementary Fig. S7.

mation is defective in human MeCP2 mutant cells [30, 72], a phenomenon we observed in NPCs depleted of *NEAT1*. Crucially, the reintroduction of *NEAT1* in *MECP2*-KO cells was able to reverse this defect (Fig. 7A). Furthermore, as our progenitor cells underwent glutamatergic differentiation, structural analysis revealed similar defects in neural complexity for *MECP2*-KO and *NEAT1*-KO cells, characterized by reduced branching (Fig. 7B and Supplementary Fig. S8A) and decreased filopodia count (Fig. 7C and Supplementary Fig. S8A). Both mutant cells exhibited shorter neurite projections, with branches and dendritic filopodia closer to the soma compared to WT cells (Fig. 7D), reminiscent of the morphological features observed in RTT neurons [73]. Considering these findings, we further evaluated the potential of *NEAT1* recovery to ameliorate the morphological phenotype of RTT neurons. Endogenous reactivation of *NEAT1* through CRISPR/SAM did not fully rescue the number of branches but did restore the total filopodia count (Fig. 7E). However, ectopic overexpression of *NEAT1* showed improvement in both aspects (Fig. 7F and Supplementary Fig. S8B), underscoring the critical role of *NEAT1* in neuronal maturation.

Overall, this study reveals the substantial role of the abundant lncRNA *NEAT1*, significantly downregulated in *MECP2* mutant cells, as a crucial downstream mediator of MeCP2 function. *NEAT1* regulates pathways controlling protein metabolism, ATG protein biogenesis, and autophagic flux. Consequently, *NEAT1* deficiency profoundly impacts ultrastructure and morphological aspects in RTT. Crucially, *NEAT1* reactivation restores autophagy and neuronal morphology, highlighting its pivotal role as a mediator of key aspects in RTT pathophysiology (Fig. 8).

Discussion

Despite significant advances in understanding MeCP2's role in the cell and the consequences of its loss of function in neurodevelopment, particularly in RTT, there is sparse literature detailing the molecular mechanisms underlying dysregulated cellular pathways in RTT. Loss of function in *MECP2* mutant cells leads to various metabolic defects, including impaired glucose and cholesterol metabolism, disrupted mitochondrial homeostasis, and redox imbalance, as observed in patients and animal models of the disorder [74–76]. One critical pathway linking MeCP2 function and cellular metabolism is mTORC1 signaling, which modulates synaptic plasticity and learning and is increasingly recognized as a hallmark of RTT across different study models [62, 77, 78]. However, the mechanistic details of how MeCP2 controls metabolic dysfunction are underdefined. In this study, we aimed to address this research gap and integrate scRNA-seq analysis, revealing significant downregulation of *NEAT1* in *MECP2* mutant cells. While single-cell transcriptomic analysis has been applied to study mosaicism in female mouse models and postmortem human Rett brain tissue [26], our study represents the first investigation of a human cellular model of RTT during early differentiation stages at the single-cell level. This allowed the identification of *NEAT1* as an important *MECP2*-regulated gene, a functional link not previously reported in RTT. Notably, in murine models of Huntington's disease and spinocerebellar ataxias, elevated *Neat1* levels were associated with proposed protective roles against cytotoxicity, with MeCP2 protein suggested to repress *Neat1* function through direct protein:RNA binding [79]. This indicates a different mechanistic scenario from the downregulation of *NEAT1* observed in *MECP2*-KO cells and underscores the positive contribution of *NEAT1* downstream of MeCP2 function in our RTT cellular model.

The significant decrease in *NEAT1* expression in *MECP2* mutant cells in both NPCs and throughout all differentiation time points assessed here is an unusual finding in RTT cells, where individual gene expression changes typically exhibit small magnitudes of misregulation [80]. In contrast, NEAT1 upregulation is also prominent in post-mortem tissue, with a fold-change of ~8 in the hippocampus (Fig. 1H). This may reflect the differences in cellular composition, as well as variations in developmental stages and the pathological environment, suggesting context-dependent regulation of NEAT1. This highlights the importance of studying different conditions and stages of neural development in RTT physiopathology. Altogether, *NEAT1* expression may play a crucial role in the neurological phenotype of RTT, supported by the high percentage (53%) of dysregulated transcripts in *MECP2*-KO progenitor cells also dysregulated in *NEAT1*-KO cells (Fig. 3D and Supplementary Fig. S3E). Similar dysregulation of *NEAT1* has been observed in other neurological diseases such as Alzheimer's disease, PD, and Huntington's disease [53, 54, 81, 82], all characterized by abnormal protein aggregation, although the specific role of *NEAT1* in these contexts remains incompletely understood. *NEAT1* is implicated in promoting the nuclear retention of TDP-43, a protein central to many proteinopathies [83], yet the mechanisms by which elevated *NEAT1* levels prevent neurodegeneration are unclear [84]. While *NEAT1* overexpression has shown neuroprotective effects in Huntington's disease [79], its inhibition appears beneficial in Alzheimer's models [85, 86]. Elucidation of *NEAT1*'s mechanism of action in the diverse neurological contexts is therefore highly relevant. Along these lines, the observed drastic downregulation of *NEAT1* in neural cells contrasts with its upregulation in the mature diseased brain and suggests dynamic changes during neurodevelopment. However, given the central role of *NEAT1* in metabolic and autophagic control, and its ability to rescue RTT morphological deficits, this upregulation may serve as a compensatory response to pathological conditions; for example, while typically absent in the healthy brain, *NEAT1_2* and associated paraspeckles are often increased in response to cellular stress and inflammation [87]. Given that RTT and neurodegenerative diseases like Alzheimer's disease or amyotrophic lateral sclerosis are associated with cellular stress, neuroinflammation, and altered RNA metabolism, *NEAT1* upregulation could serve as a protective mechanism to mitigate disease-related dysfunction and promote neuronal survival. Additionally, while *Neat1*-KO mice do not exhibit overt neurological phenotypes [88, 89], under stress conditions they display distinct behavioral defects such as decreased anxiety, hyperlocomotion, and impaired sociability [60], further highlighting the neuroprotective role of *NEAT1*.

LncRNAs have gained increased attention in neurodevelopmental diseases due to their diverse roles in maintaining cellular homeostasis [59]. Despite growing evidence linking lncRNAs to neurogenesis, neuronal differentiation, maturation, and synaptic plasticity [90, 91], the precise mechanisms by which these molecules regulate these processes, particularly their interactions with other macromolecules, remain unclear. *NEAT1*, extensively studied in tumorigenesis, functions as a structural RNA essential for forming membraneless nuclear hubs known as paraspeckles, which play

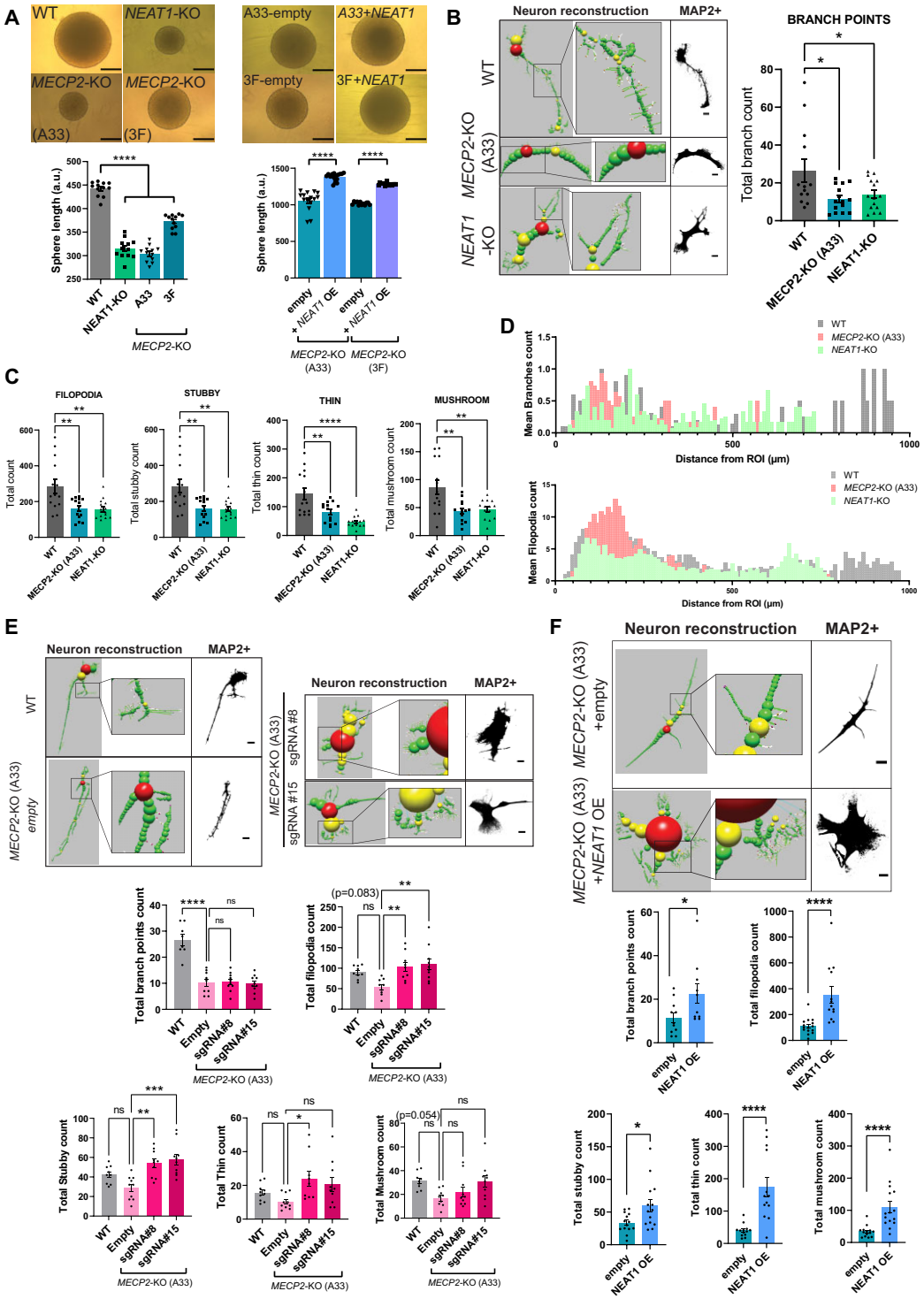

Figure 7. *NEAT1* reexpression restores the morphological defects of *MECP2*-KO neurons. (**A**) Diameter length of neurospheres was measured for WT, *NEAT1*-KO or *MeCP2*-KO (clones A33 and 3F) cells (left) and upon transfection of an empty vector or a vector carrying *NEAT1_2* (right). Graphs represent the mean ± SEM of at least 12 measurements (*****P* < .0001, one-way ANOVA). Images correspond to representative spheres of each condition. Scale bar = 0.25 mm. (**B**) (Left) Control WT neural progenitors, *MECP2*-KO (clone A33) or *NEAT1*-KO cells were driven towards glutamatergic differentiation for 7 days, stained with MAP2 and reconstructed *in silico* from confocal images with the NeuronStudio software. One representative picture for each condition is shown. (Right) Automatic analysis of the cells in (**B**) allowed total branch points count per each condition (graphs represent mean ± SEM, $n = 15$ neurons, **P* < .05, one-way ANOVA). Scale bar = 10 µm. (**C**) For the same cells as in (**B**), the total filopodia count and the abundance of each filopodia subtype was determined with the NeuronStudio software ($n = 15$ neurons, ***P* < .01, *****P* < .0001, one-way ANOVA). (**D**) The same quantification in panels (B) and (C) was represented in the histograms as distance from the soma. (**E**) Morphological analysis as in panels (B) and (C) with WT or *MECP2*-KO (clone A33) differentiated cells expressing empty vector or sgRNAs to reactivate *NEAT1*. Graphs represent mean ± SEM, $n = 10$ neurons (**P* < .05, ***P* < .01, ****P* < .001, *****P* < .0001, ns = not significant, one-way ANOVA). (**F**) Morphological analysis as in panel (**E**) with *MECP2*-KO (clone A33) differentiated cells expressing *NEAT1_2* or an empty vector as control. Graphs represent mean ± SEM, $n = 15$ neurons (**P* < .05, *****P* < .0001, two-tailed Mann–Whitney U test). See also Supplementary Fig. S8.

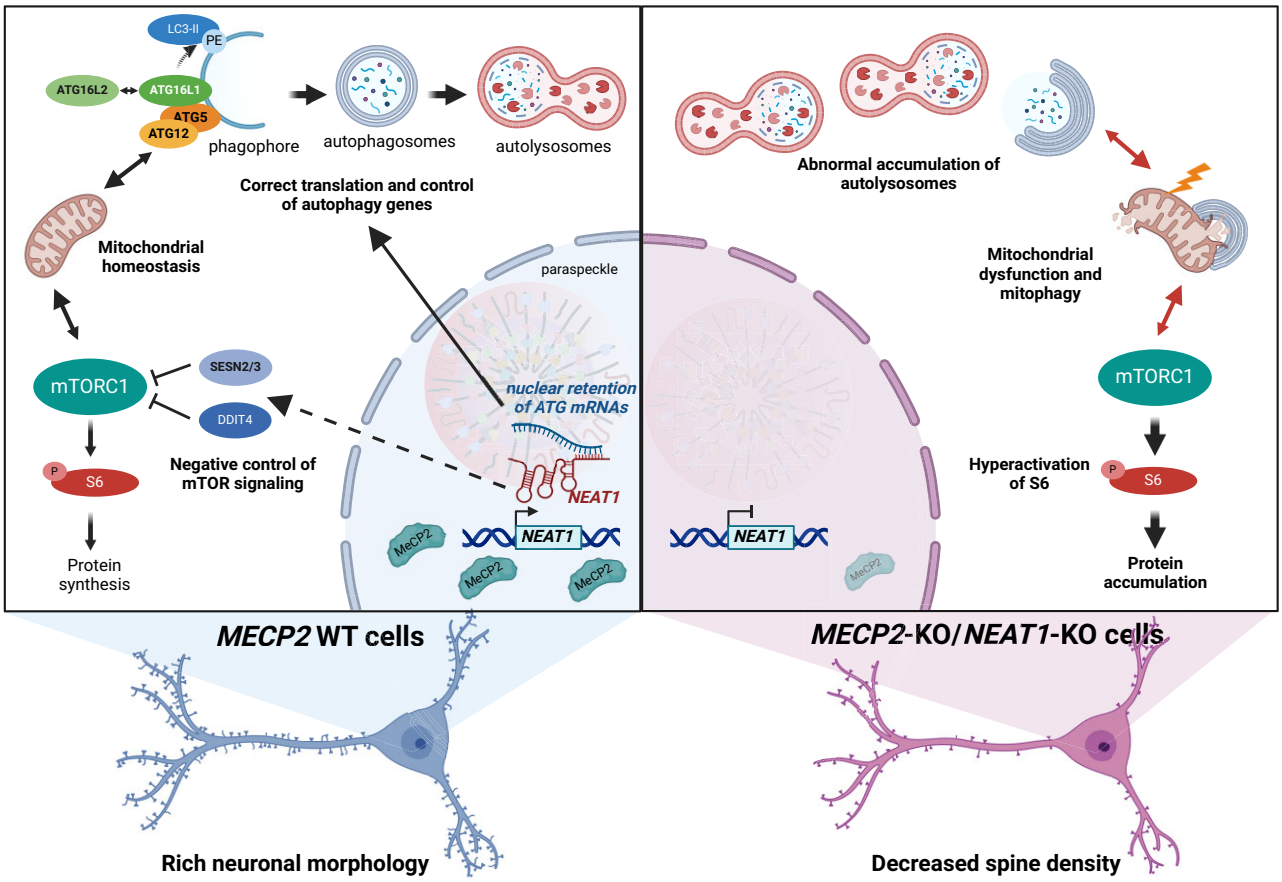

Figure 8. Schematic summarizing the findings in this work. (Left) In control NPCs, the lncRNA *NEAT1* regulates protein metabolism by reducing the activation of S6 protein through regulation of mTORC1 and by directly interacting with autophagy-related transcripts, promoting their biogenesis and translation. *NEAT1* responds to stress stimuli and positively influences the autophagic response. (Right) In *MECP2*-KO cells, the marked downregulation of *NEAT1* expression causes hyperactivation of S6 and protein accumulation. At the same time, dysregulation of autophagy-related genes results in the blockage of the autophagic flux, loss of protein homeostasis, and mitochondrial dysfunction, which can be observed at the functional and structural level. Altogether, neurons derived from mutant *NEAT1* or *MECP2* cells display similar morphological defects, which can be rescued by the reactivation of *NEAT1* expression. This suggests a central role for *NEAT1* in mediating the metabolic dysregulation typical of RTT. The dashed arrow indicates as yet unclear mechanisms of regulation. Diagram was created in BioRender. Soler (2025) https://BioRender.com/e64d138.

a crucial role in RNA biogenesis by selectively sequestering components of ribonucleoprotein complexes [92]. The nuclear retention of specific mRNAs can be paraspeckle-dependent, cellular stress-dependent [93, 94], and/or follow circadian rhythms [45, 95]. For example, several mRNAs encoding mitochondrial proteins have been found to be retained in the nucleus through direct interaction with *NEAT1*, highlighting the close relationship between mitochondrial and nuclear stresses [67]. While our data does not exclude the possibility of paraspeckle-dependent retention of ATG transcripts, further research is needed to clarify the specific roles of each *NEAT1* isoform and the potential involvement of paraspeckles in the nuclear accumulation of ATG mRNAs.

To our knowledge, this is the first report linking nuclear retention of autophagy-related transcripts to the positive regulation of corresponding protein levels. Nuclear retention of developmental or stress response genes is a known regulatory mechanism, allowing cells to modulate protein expression in response to changing conditions. Typically, when specific cues are present, these mRNAs relocate to the cytoplasm for translation, ensuring precise spatial and temporal control of gene expression [93, 96]. In contrast, cytoplasmic accumulation of ATG mRNAs in *NEAT1-KO* and *MECP2*-KO cells leads to downregulation rather than increased protein levels, suggesting that *NEAT1*-mediated nuclear retention is essential for efficient mRNA biogenesis, and/or export and translation. One intriguing possibility is that RNA modifications, such as A-to-I editing sustained by paraspeckles, or methylation, required for downstream processes in the expression route of these genes, depend on *NEAT1*-mediated nuclear retention. A limitation of our study is that we have not distinguished between the roles of the short and long *NEAT1* isoforms. Although ectopic overexpression of full-length *NEAT1_2* (22 kb) can restore neuronal morphology, it remains unclear whether the short *NEAT1_1* isoform, also generated from the same construct, also plays a role. Future studies should investigate whether paraspeckle formation per se (dependent on the long isoform but unlikely to be restored with ectopic *NEAT1_2* overexpression) is required for transcript localization and autophagy control or if these are *NEAT1*-dependent functions independent of subnuclear bodies. Equally intriguing are the sequence features on ATG mRNAs that sustain interaction with *NEAT1*. For example, we could find no evidence of Alu repeats on the nuclear-retained ATG mRNAs, a feature previously linked to retention in paraspeckles [97, 98]. Although we have identified the interaction regions between *NEAT1*

and *ATG16L2* or *ATG5* mRNAs, further research is needed to confirm the exact sequence determinants underlying *NEAT1*–mRNA interactions.

Autophagy stands as a pivotal mechanism for preserving cellular cleanliness in eukaryotic cells, orchestrating the degradation of long-lived cytoplasmic proteins, complexes, and organelles. Significantly, the autophagy–lysosomal pathway is implicated in neurodegenerative disorders, where it functions in clearing accumulated abnormal proteins like huntingtin, tau, and alpha-synuclein from within cells [99, 100]. Moreover, emerging evidence underscores the role of autophagy regulation in processes central to neurodevelopment [101]. Metabolic dysfunction, notably involving glucose and cholesterol, and redox imbalance, are well-established hallmarks of RTT [74–76, 102]. While autophagy plays a crucial role in maintaining cellular metabolic homeostasis, particularly in post-mitotic neurons, its involvement in RTT pathogenesis remains unexplored. Previous studies have indicated an association between MeCP2 and mTORC1/2 complexes and signaling, with a general reduction observed in mTOR signaling pathway [78, 103, 104]. However, some brain regions from RTT patients have shown increased mTOR protein levels and phosphorylation status, linked to ribosomal biogenesis and ribosomal RNA induction [62]. Our findings reveal activation of S6 ribosomal protein and protein accumulation in *MECP2*-KO and *NEAT1*-KO neural progenitors despite the reduction in total mTOR levels. These results partially align with previous studies in RTT iPSCs, indicating reduced global translation, compromised mTOR signaling, and impairment in ubiquitination processes leading to protein accumulation [105]. While mechanistic discrepancies exist across various model systems and cellular types, accumulating evidence suggests that dysregulated protein translation and accumulation, leading to cellular resource exhaustion, are significant burdens for *MECP2* mutant cells. Proper control of autophagy may hold the key to restoring the RTT phenotype, as the accumulation of abnormally shaped autophagosomes is a hallmark of neurodegenerative diseases and lysosomal pathologies. Despite limited focus to date on autophagy status in neurodevelopmental disorders and RTT models specifically, our study provides compelling evidence that autophagy dysregulation significantly contributes to the mutant *MECP2* phenotype. Indeed, a study has reported defects in autophagy activation and autophagosome formation in fibroblasts from RTT patients [64], providing evidence that autophagy impairment is a characteristic feature of RTT pathophysiology. Moreover, our data highlights *NEAT1* downregulation in RTT as the primary defect triggering autophagic impairment, a feature potentially applicable to other neurodevelopmental disorders.

The influence of *NEAT1* on autophagy has been documented in numerous cancer studies, where *NEAT1* is shown to promote autophagy in various tumorigenic contexts. While the precise mechanism remains largely unspecified, it is generally proposed that *NEAT1* modulates the activity of several miRNAs, ultimately impacting autophagy-related genes [106–108]. For example, in mouse hepatic stellate cells, *NEAT1* has been reported to regulate autophagy by binding directly to *miR-29b*, thereby regulating *ATG9A* expression [109]. Moreover, in myeloma, the replacement of *miR-29b* disrupts the autophagy pathway [110]. Interestingly, *miR-29b* is also highly expressed in the brain and predicted to interact with *ATG16L1* and *BECN1* (as assessed by the multiMiR 1.24.0 package [111]). Similarly, in neurodegenerative conditions such as PD and cerebral ischemia-reperfusion injury, *NEAT1* has been implicated in promoting autophagy, often via miRNA regulation or other yet unidentified mechanisms [112, 113]. While the literature supports the possibility of *NEAT1* regulating autophagy-related genes through miRNA modulation, our findings suggest a distinct role for *NEAT1* in the control of ATGs through mRNA relocation, indicating a direct RNA–RNA interaction between *NEAT1* and the mRNAs. However, considering the intricate landscape of RTT, various mechanisms may contribute significantly to the observed effects.

Our findings reveal a direct interaction between *NEAT1* and specific autophagy-related mRNAs, including *ATG16L2* and *ATG5* (Fig. 6). Interestingly, while additional autophagy proteins such as ATG12 and ATG3 are affected in *NEAT1*-deficient cells (Fig. 5), there are no quantitative changes in their mRNA localization. This suggests that *NEAT1* may selectively regulate key players to exert global control over ATG complexes. For instance, the E3 ligase complex ATG16L1-ATG5-ATG12 acts as a scaffold for the E2-like enzyme ATG3, facilitating the conjugation of LC3 to phosphatidylethanolamine and the maturation of the nascent phagophore into the autophagosome [114]. Changes in the localization of *ATG5* and *ATG16L1* mRNAs, and consequently their protein levels, are likely to influence the levels of ATG12 and ATG3 proteins, despite no significant relocalization of *ATG12* and *ATG3* mRNAs is observed in *MECP2*-KO cells. While ATG16L2, a paralog of ATG16L1, remains less studied, it has been suggested to play a potential autophagic inhibitory role by interfering with the formation of the ATG12-ATG5-ATG16L1 complex and LC3 lipidation [115]. Notably, alterations in ATG16L2 levels have been observed in several neurodegenerative diseases [116, 117], although its implications in neurodevelopment have yet to be elucidated.

Our findings also reveal *NEAT1* as a crucial negative regulator of S6 phosphorylation in NPCs, which contrasts with the typical positive correlation between *NEAT1* expression and mTOR activation observed in cancer cells [118–121]. This suggests that the role of *NEAT1* may vary depending on cell type and context. This additional layer of regulation exerted by *NEAT1* on the autophagic flux leads to impaired autophagosomal/autolysosomal ratio and disrupted autophagic dynamics in *NEAT1*-KO cells. Consequently, this disruption may result in the accumulation of misfolded or aggregated proteins and a loss of cellular protein quality control mechanisms, ultimately leading to abnormal neuronal morphology.

Our findings underscore the potential therapeutic importance of targeting *NEAT1* and autophagy as promising approaches to alleviate the molecular and cellular dysfunctions associated with RTT. This offers hope for the development of novel treatment strategies for this debilitating neurodevelopmental disorder.

Acknowledgements

We thank the CERCA program (Generalitat de Catalunya) and the Josep Carreras Foundation for institutional support and the Guil lab for discussion and help. We are grateful for the technical support provided by the CCiTUB, University of Barcelona, L'Hospitalet de Llobregat, Spain, and the Advanced Microscopy Unit, IJC, co-financed by FEDER 'A way of making Europe'. We thank the Rett Syn-

drome Research Trust for the donation of the iPSCs used in this study (ID 2037). We are indebted to the 'Biobanc de l'Hospital Infantil Sant Joan de Déu per a la Investigació', integrated in the Spanish Biobank Network of ISCIII for the sample and data procurement. Angelica Garcia (IJC) is gratefully acknowledged for her valuable technical assistance. Graphical Abstract was created in BioRender.com (Soler 2025) and can be accessed in https://BioRender.com/m66m166.

Author contributions: Conceptualization, E.S., A.L., and S.G.; Methodology, E.S., C.D.V., T.S., F.S., and L.M.-V.; Formal analysis, M.C.-P. and L.F.A.; Investigation, E.S., C.D.V., A.T., M.S., and C.O.-M.; Resources, J.A.; Writing—original draft, E.S. and S.G.; Writing—review & editing, E.S., T.S., L.F.A., A.L., and S.G.; Supervision, M.E., A.L., and S.G.; Funding acquisition, M.E., A.L., and S.G.

Supplementary data

Supplementary data is available at NAR online.

Conflict of interest

The authors declare no competing interests.

Funding

This work was supported by the Spanish Ministerio de Ciencia, Innovación y Universidades, co-funded by European Regional Development Fund, ERDF, [PID2022-142829OB-I00, AEI/10.13039/501100011033 to S.G., PID2021-124536NB-I00 to A.L., PID2021-125282OB-I00, MCIN/AEI/10.13039/501100011033/ to M.E.]; the Departament de Recerca i Universitats/Generalitat de Catalunya [2021 SGR 01309 to S.G., 2021 SGR 01494 to M.E.]; the Catalan and the Spanish Associations for Rett Syndrome [FinRett to S.G.]; the Cellex Foundation [CEL007 to M.E.]; and the Conselho Nacional de Desenvolvimento Científico e Tecnológico (CNPq, Brasilia, Brazil), 'Science without borders' scholarship [202074/2015-3 to E.S.]. M.E. is an ICREA Research Professor. Funding to pay the Open Access publication charges for this article was provided by Spanish Ministry of Science and Innovation.

Data availability

The data underlying this article are available in the European Nucleotide Archive (ENA), and can be accessed with the following accession numbers: PRJEB75396 (single-cell transcriptomic analysis of mutant *MECP2* human neural cells (*MECP2*-KO, clone A33) over a time-course of *in vitro* differentiation, https://www.ebi.ac.uk/ena/browser/view/PRJEB75396); PRJEB82130 (single-cell transcriptomic analysis of progenitor and 7 days differentiated mutant *MECP2* human neural cells (clones A33 and 3F), https://www.ebi.ac.uk/ena/browser/view/PRJEB82130); PRJEB75392 (transcriptomic analysis of mutant *MECP2* human neural progenitor cells (*MECP2*-R133C), https://www.ebi.ac.uk/ena/browser/view/PRJEB75392); PRJEB75393 (transcriptomic analysis of mutant *MECP2*-KO (clone A33) and *NEAT1*-KO human neural cells, https://www.ebi.ac.uk/ena/browser/view/PRJEB75393); PRJEB81894 (*NEAT1* RIP-seq in neural progenitor cells, https://www.ebi.ac.uk/ena/browser/view/PRJEB81894).

References

1. Ausió J, Martínez de Paz A, Esteller M. MeCP2: the long trip from a chromatin protein to neurological disorders. *Trends Mol Med* 2014;**20**:487–98. https://doi.org/10.1016/j.molmed.2014.03.004
2. Lyst MJ, Bird A. Rett syndrome: a complex disorder with simple roots. *Nat Rev Genet* 2015;**16**:261–75. https://doi.org/10.1038/nrg3897
3. Tillotson R, Bird A. The molecular basis of MeCP2 function in the brain. *J Mol Biol* 2020;**432**:1602–23. https://doi.org/10.1016/j.jmb.2019.10.004
4. Lewis JD, Meehan RR, Henzel WJ *et al.* Purification, sequence, and cellular localization of a novel chromosomal protein that binds to methylated DNA. *Cell* 1992;**69**:905–14. https://doi.org/10.1016/0092-8674(92)90610-O
5. Dragich JM, Kim YH, Arnold AP *et al.* Differential distribution of the MeCP2 splice variants in the postnatal mouse brain. *J Comp Neurol* 2007;**501**:526–42. https://doi.org/10.1002/cne.21264
6. Zhang ZN, Freitas BC, Qian H *et al.* Layered hydrogels accelerate iPSC-derived neuronal maturation and reveal migration defects caused by MeCP2 dysfunction. *Proc Natl Acad Sci USA* 2016;**113**:3185–90. https://doi.org/10.1073/pnas.1521255113
7. Lavery LA, Zoghbi HY. The distinct methylation landscape of maturing neurons and its role in Rett syndrome pathogenesis. *Curr Opin Neurobiol* 2019;**59**:180–8. https://doi.org/10.1016/j.conb.2019.08.001
8. Amir RE, Van den Veyver IB, Wan M *et al.* Rett syndrome is caused by mutations in X-linked MECP2, encoding methyl-CpG-binding protein 2. *Nat Genet* 1999;**23**:185–8. https://doi.org/10.1038/13810
9. Hagberg B, Aicardi J, Dias K *et al.* A progressive syndrome of autism, dementia, ataxia, and loss of purposeful hand use in girls: Rett's syndrome: report of 35 cases. *Ann Neurol* 1983;**14**:471–9. https://doi.org/10.1002/ana.410140412
10. Leonard H, Cobb S, Downs J. Clinical and biological progress over 50 years in Rett syndrome. *Nat Rev Neurol* 2017;**13**:37–51. https://doi.org/10.1038/nrneurol.2016.186
11. Palmieri M, Pozzer D, Landsberger N. Advanced genetic therapies for the treatment of Rett syndrome: state of the art and future perspectives. *Front Neurosci* 2023;**17**:1172805. https://doi.org/10.3389/fnins.2023.1172805
12. Panayotis N, Ehinger Y, Felix MS *et al.* State-of-the-art therapies for Rett syndrome. *Develop Med Child Neuro* 2023;**65**:162–70. https://doi.org/10.1111/dmcn.15383
13. Keam SJ. Trofinetide: first approval. *Drugs* 2023;**83**:819–24. https://doi.org/10.1007/s40265-023-01883-8
14. Katz DM, Berger-Sweeney JE, Eubanks JH *et al.* Preclinical research in Rett syndrome: setting the foundation for translational success. *Dis Model Mech* 2012;**5**:733–45. https://doi.org/10.1242/dmm.011007
15. Medrihan L, Tantalaki E, Aramuni G *et al.* Early defects of GABAergic synapses in the brain stem of a MeCP2 mouse model of Rett syndrome. *J Neurophysiol* 2008;**99**:112–21. https://doi.org/10.1152/jn.00826.2007
16. Chao HT, Zoghbi HY, Rosenmund C. MeCP2 controls excitatory synaptic strength by regulating glutamatergic synapse number. *Neuron* 2007;**56**:58–65. https://doi.org/10.1016/j.neuron.2007.08.018
17. Calfa G, Percy AK, Pozzo-Miller L. Experimental models of Rett syndrome based on Mecp2 dysfunction. *Exp Biol Med (Maywood)* 2011;**236**:3–19. https://doi.org/10.1258/ebm.2010.010261
18. Stearns NA, Schaevitz LR, Bowling H *et al.* Behavioral and anatomical abnormalities in Mecp2 mutant mice: a model for

Rett syndrome. *Neuroscience* 2007;**146**:907–21. https://doi.org/10.1016/j.neuroscience.2007.02.009
19. Ben-Reuven L, Reiner O. Modeling the autistic cell: iPSCs recapitulate developmental principles of syndromic and nonsyndromic ASD. *Dev Growth Differ* 2016;**58**:481–91. https://doi.org/10.1111/dgd.12280
20. Ran FA, Hsu PD, Wright J *et al.* Genome engineering using the CRISPR-Cas9 system. *Nat Protoc* 2013;**8**:2281–308. https://doi.org/10.1038/nprot.2013.143
21. Powell SK, Gregory J, Akbarian S *et al.* Application of CRISPR/Cas9 to the study of brain development and neuropsychiatric disease. *Mol Cell Neurosci* 2017;**82**:157–66. https://doi.org/10.1016/j.mcn.2017.05.007
22. Haase FD, Coorey B, Riley L *et al.* Pre-clinical investigation of Rett syndrome using human stem cell-based disease models. *Front Neurosci* 2021;**15**:698812. https://doi.org/10.3389/fnins.2021.698812
23. Lu S, Chen Y, Wang Z. Advances in the pathogenesis of Rett syndrome using cell models. *Anim Models and Exp Med* 2022;**5**:532–41. https://doi.org/10.1002/ame2.12236
24. Piwecka M, Rajewsky N, Rybak-Wolf A. Single-cell and spatial transcriptomics: deciphering brain complexity in health and disease. *Nat Rev Neurol* 2023;**19**:346–62. https://doi.org/10.1038/s41582-023-00809-y
25. Zito A, Lee JT. Variable expression of MECP2, CDKL5, and FMR1 in the human brain: Implications for gene restorative therapies. *Proc Natl Acad Sci USA* 2024;**121**:e2312757121. https://doi.org/10.1073/pnas.2312757121
26. Renthal W, Boxer LD, Hrvatin S *et al.* Characterization of human mosaic Rett syndrome brain tissue by single-nucleus RNA sequencing. *Nat Neurosci* 2018;**21**:1670–9. https://doi.org/10.1038/s41593-018-0270-6
27. Donato R, Miljan EA, Hines SJ *et al.* Differential development of neuronal physiological responsiveness in two human neural stem cell lines. *BMC Neurosci* 2007;**8**:36. https://doi.org/10.1186/1471-2202-8-36
28. Choi SH, Kim YH, Hebisch M *et al.* A three-dimensional human neural cell culture model of Alzheimer's disease. *Nature* 2014;**515**:274–8. https://doi.org/10.1038/nature13800
29. Choi SH, Kim YH, Quinti L *et al.* 3D culture models of Alzheimer's disease: a road map to a "cure-in-a-dish". *Mol Neurodegener* 2016;**11**:75. https://doi.org/10.1186/s13024-016-0139-7
30. Siqueira E, Obiols-Guardia A, Jorge-Torres OC *et al.* Analysis of the circRNA and T-UCR populations identifies convergent pathways in mouse and human models of Rett syndrome. *Mol Ther Nucleic Acids* 2022;**27**:621–44. https://doi.org/10.1016/j.omtn.2021.12.030
31. Siqueira E, Kim BH, Reser L *et al.* Analysis of the interplay between MeCP2 and histone H1 during *in vitro* differentiation of human ReNCell neural progenitor cells. *Epigenetics* 2023;**18**:2276425. https://doi.org/10.1080/15592294.2023.2276425
32. Klec C, Prinz F, Pichler M. Involvement of the long noncoding RNA NEAT1 in carcinogenesis. *Mol Oncol* 2019;**13**:46–60. https://doi.org/10.1002/1878-0261.12404
33. Dong P, Xiong Y, Yue J *et al.* Long non-coding RNA NEAT1: a novel target for diagnosis and therapy in human tumors. *Front Genet* 2018;**9**:471. https://doi.org/10.3389/fgene.2018.00471
34. Zhao MY, Wang GQ, Wang NN *et al.* The long-non-coding RNA NEAT1 is a novel target for Alzheimer's disease progression via miR-124/BACE1 axis. *Neurol Res* 2019;**41**:489–97. https://doi.org/10.1080/01616412.2018.1548747
35. Sunwoo JS, Lee ST, Im W *et al.* Altered expression of the long noncoding RNA NEAT1 in Huntington's disease. *Mol Neurobiol* 2017;**54**:1577–86. https://doi.org/10.1007/s12035-016-9928-9
36. Wang Z, Li K, Huang W. Long non-coding RNA NEAT1-centric gene regulation. *Cell Mol Life Sci* 2020;**77**:3769–79. https://doi.org/10.1007/s00018-020-03503-0
37. Wu H, Chen S, Li A *et al.* LncRNA expression profiles in systemic lupus erythematosus and rheumatoid arthritis: emerging biomarkers and therapeutic targets. *Front Immunol* 2021;**12**:792884. https://doi.org/10.3389/fimmu.2021.792884
38. Li R, Harvey AR, Hodgetts SI *et al.* Functional dissection of NEAT1 using genome editing reveals substantial localization of the NEAT1_1 isoform outside paraspeckles. *RNA* 2017;**23**:872–81. https://doi.org/10.1261/rna.059477.116
39. Shin VY, Chen J, Cheuk IW *et al.* Long non-coding RNA NEAT1 confers oncogenic role in triple-negative breast cancer through modulating chemoresistance and cancer stemness. *Cell Death Dis* 2019;**10**:270. https://doi.org/10.1038/s41419-019-1513-5
40. Zhu Y, Hu H, Yuan Z *et al.* LncRNA NEAT1 remodels chromatin to promote the 5-Fu resistance by maintaining colorectal cancer stemness. *Cell Death Dis* 2020;**11**:962. https://doi.org/10.1038/s41419-020-03164-8
41. Yamazaki T, Fujikawa C, Kubota A *et al.* CRISPRa-mediated NEAT1 lncRNA upregulation induces formation of intact paraspeckles. *Biochem Biophys Res Commun* 2018;**504**:218–24. https://doi.org/10.1016/j.bbrc.2018.08.158
42. Clemson CM, Hutchinson JN, Sara SA *et al.* An architectural role for a nuclear noncoding RNA: NEAT1 RNA is essential for the structure of paraspeckles. *Mol Cell* 2009;**33**:717–26. https://doi.org/10.1016/j.molcel.2009.01.026
43. Leeman DS, Hebestreit K, Ruetz T *et al.* Lysosome activation clears aggregates and enhances quiescent neural stem cell activation during aging. *Science* 2018;**359**:1277–83. https://doi.org/10.1126/science.aag3048
44. Torres M, Becquet D, Guillen S *et al.* RNA pull-down procedure to identify RNA targets of a long non-coding RNA. *J Vis Exp* 2018;**134**:57379.
45. Jacq A, Becquet D, Guillen S *et al.* Direct RNA–RNA interaction between Neat1 and RNA targets, as a mechanism for RNAs paraspeckle retention. *RNA Biol* 2021;**18**:2016–27. https://doi.org/10.1080/15476286.2021.1889253
46. Xu S, Hu E, Cai Y *et al.* Using clusterProfiler to characterize multiomics data. *Nat Protoc* 2024;**19**:3292–320. https://doi.org/10.1038/s41596-024-01020-z
47. Yu G, Wang LG, Han Y *et al.* clusterProfiler: an R package for comparing biological themes among gene clusters. *OMICS* 2012;**16**:284–7. https://doi.org/10.1089/omi.2011.0118
48. Wu T, Hu E, Xu S *et al.* clusterProfiler 4.0: A universal enrichment tool for interpreting omics data. *Innovation (Camb)* 2021;**2**:100141.
49. Kuleshov MV, Jones MR, Rouillard AD *et al.* Enrichr: a comprehensive gene set enrichment analysis web server 2016 update. *Nucleic Acids Res* 2016;**44**:W90–7. https://doi.org/10.1093/nar/gkw377
50. Jassal B, Matthews L, Viteri G *et al.* The reactome pathway knowledgebase. *Nucleic Acids Res* 2020;**48**:D498–503.
51. Kahanovitch U, Patterson KC, Hernandez R *et al.* Glial dysfunction in MeCP2 deficiency models: implications for Rett syndrome. *Int J Mol Sci* 2019;**20**:3813. https://doi.org/10.3390/ijms20153813
52. Wang Z, Zhao Y, Xu N *et al.* NEAT1 regulates neuroglial cell mediating Aβ clearance via the epigenetic regulation of endocytosis-related genes expression. *Cell Mol Life Sci* 2019;**76**:3005–18. https://doi.org/10.1007/s00018-019-03074-9
53. Simchovitz A, Hanan M, Niederhoffer N *et al.* NEAT1 is overexpressed in Parkinson's disease substantia nigra and confers drug-inducible neuroprotection from oxidative stress. *FASEB J* 2019;**33**:11223–34. https://doi.org/10.1096/fj.201900830R
54. Boros FA, Maszlag-Török R, Vécsei L *et al.* Increased level of NEAT1 long non-coding RNA is detectable in peripheral blood cells of patients with Parkinson's disease. *Brain Res* 2020;**1730**:146672. https://doi.org/10.1016/j.brainres.2020.146672
55. Barry G, Briggs JA, Hwang DW *et al.* The long non-coding RNA NEAT1 is responsive to neuronal activity and is associated with

hyperexcitability states. *Sci Rep* 2017;**7**:40127. https://doi.org/10.1038/srep40127
56. Chen Y, Chang Y, Zhou J *et al.* Inhibiting lncRNA NEAT1 facilitates the sensitization of melanoma cells to cisplatin through modulating the miR-519c-3p-MeCP2 axis. *Pathol Res Pract* 2023;**243**:154364. https://doi.org/10.1016/j.prp.2023.154364
57. Sun Q, Zhang Y, Wang S *et al.* NEAT1 decreasing suppresses Parkinson's disease progression via acting as miR-1301-3p sponge. *J Mol Neurosci* 2021;**71**:369–78. https://doi.org/10.1007/s12031-020-01660-2
58. Liu Y, Lu Z. Long non-coding RNA NEAT1 mediates the toxic of Parkinson's disease induced by MPTP/MPP+ via regulation of gene expression. *Clin Exp Pharma Physio* 2018;**45**:841–8. https://doi.org/10.1111/1440-1681.12932
59. Srinivas T, Mathias C, Oliveira-Mateos C *et al.* Roles of lncRNAs in brain development and pathogenesis: Emerging therapeutic opportunities. *Mol Ther* 2023;**31**:1550–61. https://doi.org/10.1016/j.ymthe.2023.02.008
60. Kukharsky MS, Ninkina NN, An H *et al.* Long non-coding RNA Neat1 regulates adaptive behavioural response to stress in mice. *Transl Psychiatry* 2020;**10**:171. https://doi.org/10.1038/s41398-020-0854-2
61. Malagelada C, López-Toledano MA, Willett RT *et al.* RTP801/REDD1 regulates the timing of cortical neurogenesis and neuron migration. *J Neurosci* 2011;**31**:3186–96. https://doi.org/10.1523/JNEUROSCI.4011-10.2011
62. Olson CO, Pejhan S, Kroft D *et al.* MECP2 mutation interrupts nucleolin-mTOR-P70S6K signaling in Rett syndrome patients. *Front Genet* 2018;**9**:635. https://doi.org/10.3389/fgene.2018.00635
63. Konermann S, Brigham MD, Trevino AE *et al.* Genome-scale transcriptional activation by an engineered CRISPR-Cas9 complex. *Nature* 2015;**517**:583–8. https://doi.org/10.1038/nature14136
64. Sbardella D, Tundo GR, Campagnolo L *et al.* Retention of mitochondria in mature human red blood cells as the result of autophagy impairment in Rett syndrome. *Sci Rep* 2017;**7**:12297. https://doi.org/10.1038/s41598-017-12069-0
65. Zuliani I, Urbinati C, Valenti D *et al.* The anti-diabetic drug metformin rescues aberrant mitochondrial activity and restrains oxidative stress in a female mouse model of Rett syndrome. *J Clin Med*. 2020;**9**:1669. https://doi.org/10.3390/jcm9061669
66. Valenti D, de Bari L, De Filippis B *et al.* Mitochondrial dysfunction as a central actor in intellectual disability-related diseases: an overview of Down syndrome, autism, Fragile X and Rett syndrome. *Neurosci Biobehav Rev* 2014;**46**:202–17. https://doi.org/10.1016/j.neubiorev.2014.01.012
67. Wang Y, Hu SB, Wang MR *et al.* Genome-wide screening of NEAT1 regulators reveals cross-regulation between paraspeckles and mitochondria. *Nat Cell Biol* 2018;**20**:1145–58. https://doi.org/10.1038/s41556-018-0204-2
68. Mann M, Wright PR, Backofen R. IntaRNA 2.0: enhanced and customizable prediction of RNA–RNA interactions. *Nucleic Acids Res* 2017;**45**:W435–9. https://doi.org/10.1093/nar/gkx279
69. Wright PR, Georg J, Mann M *et al.* CopraRNA and IntaRNA: predicting small RNA targets, networks and interaction domains. *Nucleic Acids Res* 2014;**42**:W119–23. https://doi.org/10.1093/nar/gku359
70. Busch A, Richter AS, Backofen R. IntaRNA: efficient prediction of bacterial sRNA targets incorporating target site accessibility and seed regions. *Bioinformatics* 2008;**24**:2849–56. https://doi.org/10.1093/bioinformatics/btn544
71. Raden M, Ali SM, Alkhnbashi OS *et al.* Freiburg RNA tools: a central online resource for RNA-focused research and teaching. *Nucleic Acids Res* 2018;**46**:W25–9. https://doi.org/10.1093/nar/gky329
72. Trujillo CA, Adams JW, Negraes PD *et al.* Pharmacological reversal of synaptic and network pathology in human MECP2-KO neurons and cortical organoids. *EMBO Mol Med* 2021;**13**:e12523. https://doi.org/10.15252/emmm.202012523
73. Ip JPK, Mellios N, Sur M. Rett syndrome: insights into genetic, molecular and circuit mechanisms. *Nat Rev Neurosci* 2018;**19**:368–82. https://doi.org/10.1038/s41583-018-0006-3
74. Buchovecky CM, Turley SD, Brown HM *et al.* A suppressor screen in Mecp2 mutant mice implicates cholesterol metabolism in Rett syndrome. *Nat Genet* 2013;**45**:1013–20. https://doi.org/10.1038/ng.2714
75. Can K, Menzfeld C, Rinne L *et al.* Neuronal redox-imbalance in Rett syndrome affects mitochondria as well as cytosol, and is accompanied by intensified mitochondrial O_2 consumption and ROS release. *Front Physiol* 2019;**10**:479. https://doi.org/10.3389/fphys.2019.00479
76. Vuu YM, Roberts CT, Rastegar M. MeCP2 is an epigenetic factor that links DNA methylation with brain metabolism. *Int J Mol Sci* 2023;**24**:4218. https://doi.org/10.3390/ijms24044218
77. Pitcher MR, Herrera JA, Buffington SA *et al.* Rett syndrome like phenotypes in the R255X Mecp2 mutant mouse are rescued by MECP2 transgene. *Hum Mol Genet* 2015;**24**:2662–72. https://doi.org/10.1093/hmg/ddv030
78. Li Y, Wang H, Muffat J *et al.* Global transcriptional and translational repression in human-embryonic-stem-cell-derived Rett syndrome neurons. *Cell Stem Cell* 2013;**13**:446–58. https://doi.org/10.1016/j.stem.2013.09.001
79. Cheng C, Spengler RM, Keiser MS *et al.* The long non-coding RNA NEAT1 is elevated in polyglutamine repeat expansion diseases and protects from disease gene-dependent toxicities. *Hum Mol Genet* 2018;**27**:4303–14.
80. Gabel HW, Kinde B, Stroud H *et al.* Disruption of DNA-methylation-dependent long gene repression in Rett syndrome. *Nature* 2015;**522**:89–93. https://doi.org/10.1038/nature14319
81. Johnson R. Long non-coding RNAs in Huntington's disease neurodegeneration. *Neurobiol Dis* 2012;**46**:245–54. https://doi.org/10.1016/j.nbd.2011.12.006
82. Wu J, Chen L, Zheng C *et al.* Co-expression network analysis revealing the potential regulatory roles of lncRNAs in Alzheimer's disease. *Interdiscip Sci Comput Life Sci* 2019;**11**:645–54. https://doi.org/10.1007/s12539-019-00319-w
83. Wang C, Duan Y, Duan G *et al.* Stress induces dynamic, cytotoxicity-antagonizing TDP-43 nuclear bodies via paraspeckle lncRNA NEAT1-mediated liquid–liquid phase separation. *Mol Cell* 2020;**79**:443–58. https://doi.org/10.1016/j.molcel.2020.06.019
84. Sekar D, Tusubira D, Ross K. TDP-43 and NEAT long non-coding RNA: Roles in neurodegenerative disease. *Front Cell Neurosci* 2022;**16**:954912. https://doi.org/10.3389/fncel.2022.954912
85. Huang Z, Zhao J, Wang W *et al.* Depletion of lncRNA NEAT1 rescues mitochondrial dysfunction through NEDD4L-dependent PINK1 degradation in animal models of Alzheimer's disease. *Front Cell Neurosci* 2020;**14**:28. https://doi.org/10.3389/fncel.2020.00028
86. Li Y, Fan H, Ni M *et al.* Targeting lncRNA NEAT1 hampers Alzheimer's disease progression. *Neuroscience* 2023;**529**:88–98. https://doi.org/10.1016/j.neuroscience.2023.02.016
87. McCluggage F, Fox AH. Paraspeckle nuclear condensates: global sensors of cell stress? *Bioessays* 2021;**43**:e2000245. https://doi.org/10.1002/bies.202000245
88. Nakagawa S, Shimada M, Yanaka K *et al.* The lncRNA Neat1 is required for corpus luteum formation and the establishment of pregnancy in a subpopulation of mice. *Development* 2014;**141**:4618–27. https://doi.org/10.1242/dev.110544
89. Standaert L, Adriaens C, Radaelli E *et al.* The long noncoding RNA Neat1 is required for mammary gland development and lactation. *RNA* 2014;**20**:1844–9. https://doi.org/10.1261/rna.047332.114

90. Andersen RE, Lim DA. Forging our understanding of lncRNAs in the brain. *Cell Tissue Res* 2018;**371**:55–71. https://doi.org/10.1007/s00441-017-2711-z
91. Ng SY, Lin L, Soh BS *et al.* Long noncoding RNAs in development and disease of the central nervous system. *Trends Genet* 2013;**29**:461–8. https://doi.org/10.1016/j.tig.2013.03.002
92. Smith KP, Hall LL, Lawrence JB. Nuclear hubs built on RNAs and clustered organization of the genome. *Curr Opin Cell Biol* 2020;**64**:67–76. https://doi.org/10.1016/j.ceb.2020.02.015
93. Prasanth KV, Prasanth SG, Xuan Z *et al.* Regulating gene expression through RNA nuclear retention. *Cell* 2005;**123**:249–63. https://doi.org/10.1016/j.cell.2005.08.033
94. Chen LL, DeCerbo JN, Carmichael GG. Alu element-mediated gene silencing. *EMBO J* 2008;**27**:1694–705. https://doi.org/10.1038/emboj.2008.94
95. Torres M, Becquet D, Blanchard MP *et al.* Circadian RNA expression elicited by 3′-UTR IRAlu-paraspeckle associated elements. *eLife* 2016;**5**:e14837. https://doi.org/10.7554/eLife.14837
96. Wegener M, Müller-McNicoll M. Nuclear retention of mRNAs – quality control, gene regulation and human disease. *Semin Cell Dev Biol* 2018;**79**:131–42. https://doi.org/10.1016/j.semcdb.2017.11.001
97. Hu SB, Xiang JF, Li X *et al.* Protein arginine methyltransferase CARM1 attenuates the paraspeckle-mediated nuclear retention of mRNAs containing IRAlus. *Genes Dev* 2015;**29**:630–45. https://doi.org/10.1101/gad.257048.114
98. Chen LL, Carmichael GG. Altered nuclear retention of mRNAs containing inverted repeats in human embryonic stem cells: functional role of a nuclear noncoding RNA. *Mol Cell* 2009;**35**:467–78. https://doi.org/10.1016/j.molcel.2009.06.027
99. Fujikake N, Shin M, Shimizu S. Association between autophagy and neurodegenerative diseases. *Front Neurosci* 2018;**12**:255. https://doi.org/10.3389/fnins.2018.00255
100. Griffey CJ, Yamamoto A. Macroautophagy in CNS health and disease. *Nat Rev Neurosci* 2022;**23**:411–27. https://doi.org/10.1038/s41583-022-00588-3
101. Stavoe AKH, Holzbaur ELF. Autophagy in neurons. *Annu Rev Cell Dev Biol* 2019;**35**:477–500. https://doi.org/10.1146/annurev-cellbio-100818-125242
102. Villemagne PM, Naidu S, Villemagne VL *et al.* Brain glucose metabolism in Rett syndrome. *Pediatr Neurol* 2002;**27**:117–22. https://doi.org/10.1016/S0887-8994(02)00399-5
103. Tsujimura K, Irie K, Nakashima H *et al.* miR-199a links MeCP2 with mTOR signaling and its dysregulation leads to Rett syndrome phenotypes. *Cell Rep* 2015;**12**:1887–901. https://doi.org/10.1016/j.celrep.2015.08.028
104. Ricciardi S, Boggio EM, Grosso S *et al.* Reduced AKT/mTOR signaling and protein synthesis dysregulation in a Rett syndrome animal model. *Hum Mol Genet* 2011;**20**:1182–96. https://doi.org/10.1093/hmg/ddq563
105. Rodrigues DC, Mufteev M, Weatheritt RJ *et al.* Shifts in ribosome engagement impact key gene sets in neurodevelopment and ubiquitination in Rett syndrome. *Cell Rep* 2020;**30**:4179–96. https://doi.org/10.1016/j.celrep.2020.02.107
106. Tan W, Yuan Y, Huang H *et al.* Comprehensive analysis of autophagy related long non-coding RNAs in prognosis, immunity, and treatment of muscular invasive bladder cancer. *Sci Rep* 2022;**12**:11242. https://doi.org/10.1038/s41598-022-13952-1
107. Li X, Zhou Y, Yang L *et al.* LncRNA NEAT1 promotes autophagy via regulating miR-204/ATG3 and enhanced cell resistance to sorafenib in hepatocellular carcinoma. *J Cell Physiol* 2020;**235**:3402–13. https://doi.org/10.1002/jcp.29230
108. Lv Y, Liu Z, Huang J *et al.* LncRNA nuclear-enriched abundant transcript 1 regulates hypoxia-evoked apoptosis and autophagy via mediation of microRNA-181b. *Mol Cell Biochem* 2020;**464**:193–203. https://doi.org/10.1007/s11010-019-03660-2
109. Kong Y, Huang T, Zhang H *et al.* The lncRNA NEAT1/miR-29b/Atg9a axis regulates IGFBPrP1-induced autophagy and activation of mouse hepatic stellate cells. *Life Sci* 2019;**237**:116902. https://doi.org/10.1016/j.lfs.2019.116902
110. Jagannathan S, Vad N, Vallabhapurapu S *et al.* MiR-29b replacement inhibits proteasomes and disrupts aggresome+autophagosome formation to enhance the antimyeloma benefit of bortezomib. *Leukemia* 2015;**29**:727–38. https://doi.org/10.1038/leu.2014.279
111. Ru Y, Kechris KJ, Tabakoff B *et al.* The multiMiR R package and database: integration of microRNA-target interactions along with their disease and drug associations. *Nucleic Acids Res* 2014;**42**:e133. https://doi.org/10.1093/nar/gku631
112. Dong L, Zheng Y, Luo X. lncRNA NEAT1 promotes autophagy of neurons in mice by impairing miR-107-5p. *Bioengineered* 2022;**13**:12261–74. https://doi.org/10.1080/21655979.2022.2062989
113. Xia W, Ni X, Su Q *et al.* The lncRNA NEAT1 mediates neuronal cell autophagy and related protein expression after cerebral ischemia–reperfusion injury. *Neurochem Res* 2023;**48**:1491–503. https://doi.org/10.1007/s11064-022-03841-4
114. Bingol B. Autophagy and lysosomal pathways in nervous system disorders. *Mol Cell Neurosci* 2018;**91**:167–208. https://doi.org/10.1016/j.mcn.2018.04.009
115. Don Wai Luu L, Kaakoush NO, Castaño-Rodríguez N. The role of ATG16L2 in autophagy and disease. *Autophagy* 2022;**18**:2537–46. https://doi.org/10.1080/15548627.2022.2042783
116. Caberlotto L, Nguyen TP, Lauria M *et al.* Cross-disease analysis of Alzheimer's disease and type-2 Diabetes highlights the role of autophagy in the pathophysiology of two highly comorbid diseases. *Sci Rep* 2019;**9**:3965. https://doi.org/10.1038/s41598-019-39828-5
117. Yin L, Liu J, Dong H *et al.* Autophagy-related gene16L2, a potential serum biomarker of multiple sclerosis evaluated by bead-based proteomic technology. *Neurosci Lett* 2014;**562**:34–8. https://doi.org/10.1016/j.neulet.2013.12.070
118. Huang S, Xu Y, Ge X *et al.* Long noncoding RNA NEAT1 accelerates the proliferation and fibrosis in diabetic nephropathy through activating Akt/mTOR signaling pathway. *J Cell Physiol* 2019;**234**:11200–7. https://doi.org/10.1002/jcp.27770
119. Li B, Gu W, Zhu X. NEAT1 mediates paclitaxel-resistance of non-small cell of lung cancer through activation of Akt/mTOR signalling pathway. *J Drug Targeting* 2019;**27**:1061–7. https://doi.org/10.1080/1061186X.2019.1585437
120. Zhang X, Guan MX, Jiang QH *et al.* NEAT1 knockdown suppresses endothelial cell proliferation and induces apoptosis by regulating miR 638/AKT/mTOR signaling in atherosclerosis. *Oncol Rep* 2020;**44**:115–25. https://doi.org/10.3892/or.2020.7605
121. Yu H, Xu A, Wu B *et al.* Long noncoding RNA NEAT1 promotes progression of glioma as a ceRNA by sponging miR-185-5p to stimulate DNMT1/mTOR signaling. *J Cell Physiol* 2021;**236**:121–30. https://doi.org/10.1002/jcp.29644

Received: April 29, 2024. **Revised:** January 21, 2025. **Editorial Decision:** January 22, 2025. **Accepted:** January 28, 2025
© The Author(s) 2025. Published by Oxford University Press on behalf of Nucleic Acids Research.
This is an Open Access article distributed under the terms of the Creative Commons Attribution-NonCommercial License (https://creativecommons.org/licenses/by-nc/4.0/), which permits non-commercial re-use, distribution, and reproduction in any medium, provided the original work is properly cited. For commercial re-use, please contact reprints@oup.com for reprints and translation rights for reprints. All other permissions can be obtained through our RightsLink service via the Permissions link on the article page on our site—for further information please contact journals.permissions@oup.com.